NTNU

Norwegian University of
Science and Technology

Failure Assessment of Additively Manufacturing PLA Specimens Using an Energy-Based Criterion

Tobias Fjelldal

Preface

This Masters thesis has been written in the spring of 2018 at the Department of Engineering Design and Materials at the Norwegian University of Science and Technology with *Filippo Berto* as supervisor. It is the culmination of work conducted during the semester, as well as a literature study conducted in the fall of 2017.

Trondheim, June 2018

Tobias R. Fjelldal

Abstract

The field of additive manufacturing (AM) has in the last decades become more and more relevant. Rapid prototyping is a cheap and quick way of creating physical 3D-models of complex geometries. In this thesis, failure of polyactide (PLA) specimens created using fused deposition modelling (FDM) has been studied using an energy-based approach. PLA is a polymer created from biomass. It is therefore biodegradable and popular in the field of medical equipment. Failure loads of 12 different notched specimens has been predicted using the averaged strain energy density (ASED) obtained from numerical analyses over a control radius in the vicinity of the notch. The results indicate a good correlation between the experimental and analytical results, providing results which for the most part stay within a scatter band of $\pm 20\%$.

Sammendrag

I denne oppgaven har et energi-basert brudd-kriterie blitt brukt til å vurdere prøvestykker med forskjellige kjerver laget ved hjelp av additiv tilvirkning. Materialet som blir brukt er polyaktid (PLA) som er en biologisk nedbrytbar polymer som kan lages av flere forskjellige typer biologisk masse.

Den gjennomsnittlige tøyningsenergi-tettheten fra numeriske analyser over en kontroll-radius i umiddelbar nærhet av kjervene har blitt sammenlignet med en kritisk verdi basert på materialegenskaper for å forutsi brudd-styrken. I tillegg, har bruddstyrken blitt anslått ved bruk av stressintensitets-faktorer beregnet ved hjelp av numeriske analyser. Disse verdiene har blitt sammenlignet med resultater fra eksperimenter som har blitt gjennomført tidligere.

Resultatene fra disse analysene viser en god korrelasjon mellom de analytiske og eksperimentelle verdiene. Tallene ligger for det meste innenfor for et avvik på $\pm 20\%$. Dette regnes som innenfor hva som kan forventes av lineær-elastisk bruddmekanikk. Spesielt ved bruk av anisotropiske materialer, som additivt tilvirket PLA.

Table of Contents

List of Tables

List of Figures

Abbreviations

3PB	=	3 point bending
AM	=	Additive manufacturing
ASED	=	Average strain energy density
BC	=	Boundary conditions
DOF	=	Degrees of freedom
FEA	=	Finite element analysis
FDM	=	Fused deposition modelling
LEFM	=	Linear elastic fracture mechanics
NSIF	=	Notch stress intensity factor
PLA	=	Polyactide
SEM	=	Scanning electron microscopy
TCD	=	Theory of critical distance
UTS	=	Ultimate tensile strength

1 | Introduction

1.1 Background and Motivation

A study into the use of the theory of critical distance to predict the fracture load of notched additively manufactured PLA specimens has been conducted by Ahmed and Susmel (2018). The method proved to work quite well, despite the anisotropy and other influential factors creating uncertainties in the calculations.

For the last 20 years, an energy-based criterion has been developed as a tool for failure assessment of notched geometries. It started as a criterion for static loads in sharp notches or cracks but has developed into a criterion which can be applied to many different types of notches. Blunt and sharp notches, and static as well as cyclic loading are all compatible with the criterion.

The previous semester the thesis author worked on getting to know the failure criterion based on averaging the strain energy density over a control radius, which was developed by Lazzarin and Zambardi (2001). However, this was conducted on sharp notches and cracks, which is not the case in the specimens tested by Ahmed and Susmel (2018).

1.2 Problem Description

The ASED approach has its limitations, for instance when it comes to ductile materials. Several accurate material properties are also needed, which can be difficult to obtain in some cases. The general understanding of energy approaches applied to AM specimens is low. Therefore, studying the applicability of the approach to geometries created through AM techniques is wanted.

1.3 Project Scope

1.3.1 Objectives

The objective of this thesis is to provide a better understanding and study the feasibility of the ASED approach to predicting failure in notched AM PLA specimens. This is to be done by using the test results from Ahmed and Susmel (2018),

where 12 different notched specimens have been tested under both uniaxial tensile loading as well as 3 point bending.

The testing setups of the specimens are to be simulated in the CAE software Abaqus. All the simulations are conducted in 2D, due to the plane conditions. The results obtained from Abaqus are then to be compared to the experimental results. As well as the ASED approach, the notch stress intensity factors are to be obtained from the the specimens using Abaqus. These are to be compared to the experimental results, and the feasibility of the approach is to be assessed based on these results.

1.3.2 Limitations

Reproducing the samples, or creating new test samples in the same material and with the same method, is difficult when the goal is similar material properties. The samples have been printed using fused deposition modelling. The material properties obtained in the specimens, are dependent on several factors. Mainly the material properties of pure PLA, but also printing speed, nozzle diameter and nozzle temperature are all factors which affect the material properties of the specimens. This means that if one was to either reproduce the experiments, or conduct further testing of similar samples, this could prove difficult.

1.4 Thesis Structure

Chapter 2 presents most of the theory which is deemed necessary to understand the calculations conducted in the thesis.

Chapter 3 goes through three articles which are all important to this thesis. The article which lays the groundwork for the work conducted in this thesis is presented, as well as two other which presents the energy-based approach applied to different cases.

Chapter 4 presents the analyses. It goes through the setup, including model and mesh details, boundary conditions, and the outputs, as well as the results. The results obtained from the ASED and NSIF analyses, as well as the results from both criterions are compared to the experimental results. Both graphs and tables are used to make it easier for the reader to understand.

Chapter 5 contains the discussion of the results obtained from the previous chapter. The influential factors and abnormalities are presented and discussed.

Chapter 6 is the conclusion of the thesis. Here, the major points are gone through, and further work is suggested.

2 | Theory

2.1 Linear Elastic Fracture Mechanics

Linear elastic fracture mechanics is the name for a collection of methods to asses geometries subjected to stresses in the elastic regime. In the following sections, some of the most important terms, and methods which are important to the work conducted in this thesis are explained.

2.1.1 The Basics

Stress

Stress is defined as force per unit area: $\sigma = \frac{F}{A}$. In most of linear elastic fracture mechanics, the stress in a specimen is the deciding factor of the mechanisms that the specimen will experience. The behaviour of a material subjected to stresses is described as either elastic or plastic. The elastic area is where a given geometry will go back to its original shape after loading, plastic is where permanent deformations occur. In figure 2.1 a typical stress strain curve for a ductile metal is presented. The stress strain curve is the basis for most of LEFM. The curve can directly give the factors yield strength, ultimate tensile strength, and fracture point, along with several other material properties. These three however, are the most used. The yield strength is the stress at which plastic deformation will occur if loaded above this point. The UTS is the highest amount of stress a material can experience before necking occurs for elastic materials, and fracture for predominantly brittle materials. The fracture point is the stress at which fracture will occur.

The stress strain curve presented here is a curve showing the engineering stresses and strains. These values do not take into consideration the test subject changing shape during the tensile testing. A true stress true strain curve will often have a shape which continues upward around the UTS point. This fact is important when considering plasticity in the material, but in the elastic regime, engineering and true stresses and strains are very close to each other. In this paper, only loading in the elastic regime is considered, so this fact will not make a difference.

Strain

Strain is a unitless description of the amount of deformation a specimen is subjected to. For a beam with constant cross-section subjected to tensile load in the
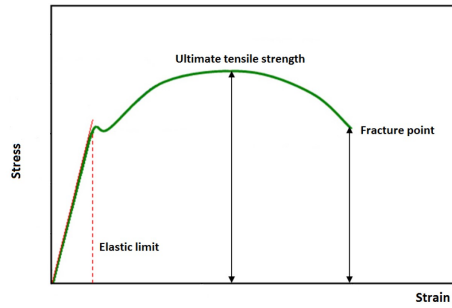
Figure 2.1: Stress strain curve of a high strength steel. (From Otani et al. (2015))

longitudinal direction, the engineering strain is given as the change in length divided by the the original length ($\Delta L/L$) (Anderson (2005)).

Young's modulus
Young's modulus, together with the Poisson's ratio are factors describing the elastic behaviour of a material. Young's modulus is often denoted as the elastic modulus (E modulus). The Young's modulus describes the relation between the stress and the strain according to Hooke's law ($\sigma = Ee$), and is a measure of the stiffness of a material within the elastic region (Otani et al. (2015)). As can be seen by re-arranging Hooke's law, the E-modulus is given by the slope of the stress strain curve in the elastic region ($E = \sigma/e$). This formulation of Hooke's law is a simplification of the general statement for uniaxial load cases. The full statement can be seen in equation 2.1, which includes multiaxial loading.

$$e_x = (1/E)[\sigma_x - \nu(\sigma_y + \sigma_z)] \tag{2.1}$$

Poisson's ratio
The Poisson's ratio is a measure of how deformation in one direction will affect the deformation in a perpendicular direction. Deformations, as explained earlier, is quantified as strain in material sciences. For a sample subjected to uniaxial tensile load along the x-direction, equation 2.2 gives the relation of strains in y- and z-direction as a function of Poisson's ratio and strain in x-direction. By re-arranging this equation, a simple definition of the Poisson's ratio can be obtained as shown. However, a simple uniaxial load case is not always the case. In those cases, the full statement from equation 2.1 is necessary (Hosford (2005)).

$$e_y = e_z = -\nu e_x \rightarrow \nu = -\frac{e_y}{e_x} = -\frac{e_z}{e_x} \tag{2.2}$$

2.1.2 Notch Stress Intensity Factors

When a crack is subjected to tensile loads, it will experience either mode I, II or III or a combination of the three. The three modes describe the different driv-

ing mechanisms behind crack growth. Each of the modes will result in different fractures, and therefore different forces to achieve crack growth.
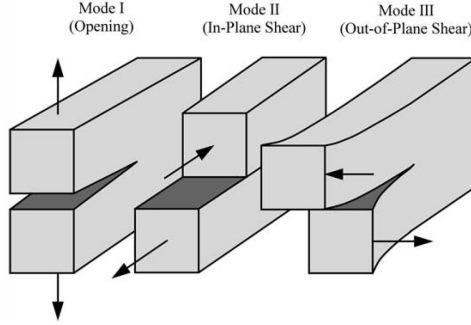
Figure 2.2: Modes I, II, and III. (From Anderson (2005))

The NSIF is a factor which describes the conditions at the near vicinity of the crack tip for linear elastic materials. Equation 2.3 introduces the parameters included in the NSIF in its simplest form for a crack subjected to solely mode I loading. The factors in question are applied stress and crack length. This equation is relevant for semi-infinite bodies, where $W >> a$, where W is the width of the plate. For specimens that don't fulfill this demand, a factor f is used. The factor f is a function of a and W, as well the position of the crack.

$$K_I = \sigma \sqrt{\pi a} \tag{2.3}$$

If K_I is known and only mode I loading is applied, the stress situation at positions around the crack-tip can be decided using equations 2.4, 2.5 and 2.6. In cases that combine other modes, several other factors have to be taken into account. In this thesis, only mode I loading is used. Figure 2.3 shows the parameters used in the stress equations.

$$\sigma_{xx} = \frac{K_I}{\sqrt{2\pi r}} \cos\left(\frac{\theta}{2}\right) \left[1 - \sin\left(\frac{\theta}{2}\right) \sin\left(\frac{3\theta}{2}\right)\right] \tag{2.4}$$

$$\sigma_{yy} = \frac{K_I}{\sqrt{2\pi r}} \cos\left(\frac{\theta}{2}\right) \left[1 + \sin\left(\frac{\theta}{2}\right) \sin\left(\frac{3\theta}{2}\right)\right] \tag{2.5}$$

$$\tau_{xy} = \frac{K_I}{\sqrt{2\pi r}} \cos\left(\frac{\theta}{2}\right) \sin\left(\frac{\theta}{2}\right) \cos\left(\frac{3\theta}{2}\right) \tag{2.6}$$

For calculations of the NSIF's caused by a notch with a notch radius ρ, a method was presented by Lazzarin and Filippi (2006). This method is also useful for mixed mode problems. The method is based on the general equation for K_I shown in equation 2.3. This equation is only valid for cracks, so to be able to numerically calculate the NSIF's equation 2.7 is used. r_0 is the distance from the notch tip to the coordinate systems origin, as shown in figure 2.4. This is dependent on the notch opening angle 2α and notch radius ρ. For notch opening angles equal to zero,
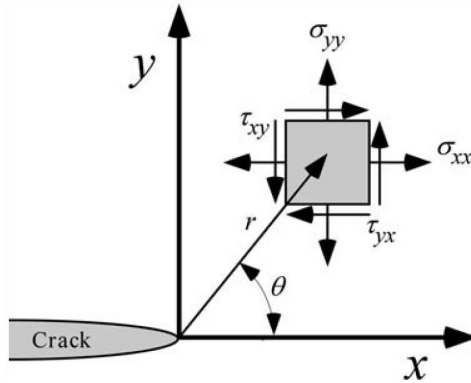
Figure 2.3: Stress distribution in the near vicinity of a crack tip as a function of K_1 given in polar coordinates. (From Anderson (2005))

the r_0 is equal to half the notch radius. It is also worth to mention the factor r is the distance from the coordinate system origin, and not the notch tip.

$$K_{\rho,I}^V = \sqrt{2\pi} r^{1-\lambda_1} \frac{(\sigma_\theta)_{\theta=0}}{1 + \widetilde{\omega}_1 \left(\frac{r}{r_0}\right)^{\mu_1-\lambda_1}} \tag{2.7}$$

The values for σ_θ are plotted along the notch bisector line from FEA software. the factors λ_1, μ_1 and $\widetilde{\omega}_1$ are all dependent on the notch opening angle.
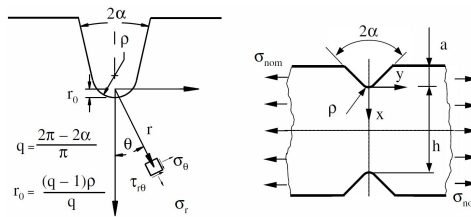
Figure 2.4: local coordinate system for blunt notches. (From Lazzarin and Filippi (2006))

2.1.3   Strain Energy Density

Any specimen or geometry experiencing strain has an equivalent energy state which is a direct function of the amount of strain the specimen is under. For FEA software to calculate the strain energy, it takes into consideration the nodal displacement which directly correlates to the amount of strain the specimen is under.

Because strain energy is in direct correlation with the loading conditions, it can be used to give an understanding of the stress state around a crack or notch. This information can in turn be used to calculate fracture load or fatigue behaviour of different geometries.

Equation 2.8 shows how the strain energy density can be calculated in materials under a linear elastic regime (Lazzarin and Zambardi (2001)). For sharp V-notches, the stress distribution with respect to the bisector line is presented in equation 2.9. The factor λ_1 is the Williams eigenvalues (Williams (1952)) for mode I cases, while the factor χ_1 is a notch opening angle dependent factor.

$$W(r,\theta) = \frac{1}{2E}\{\sigma_{11}^2 + \sigma_{22}^2 + \sigma_{33}^2 - 2\nu(\sigma_{11}\sigma_{22} + \sigma_{11}\sigma_{33} + \sigma_{22}\sigma_{33}) + 2(1+\nu)\sigma_{12}^2\} \quad (2.8)$$

$$\begin{Bmatrix} \sigma_{\theta\theta} \\ \sigma_{rr} \\ \sigma_{r\theta} \end{Bmatrix} = \frac{1}{\sqrt{2\pi}} \frac{r^{\lambda_1-1}K_1}{(1+\lambda_1)+\chi_1(1-\lambda_1)}$$
$$\cdot \left[\begin{Bmatrix} (1+\lambda_1)\cos(1-\lambda_1)\theta \\ (3-\lambda_1)\cos(1-\lambda_1)\theta \\ (1-\lambda_1)\sin(1-\lambda_1)\theta \end{Bmatrix} + \chi_1(1-\lambda_1) \begin{Bmatrix} \cos(1+\lambda_1)\theta \\ -\cos(1+\lambda_1)\theta \\ \sin(1+\lambda_1)\theta \end{Bmatrix} \right] \quad (2.9)$$

The method of using a local energy based criterion for the prediction of static and fatigue problems in notches with varying opening angles was proposed by Lazzarin and Zambardi (2001). It is based on the assumption that a material will fail when the averaged strain energy density inside a certain volume reaches a critical value W_c. Calculations of the critical strain energy density and the control radius depend both on material properties. According to Aliha et al. (2017), the method was first applied to sharp V-notches under in-plane mixed mode loading conditions. However, the method was soon developed, and is now applicable for several notch types and materials.
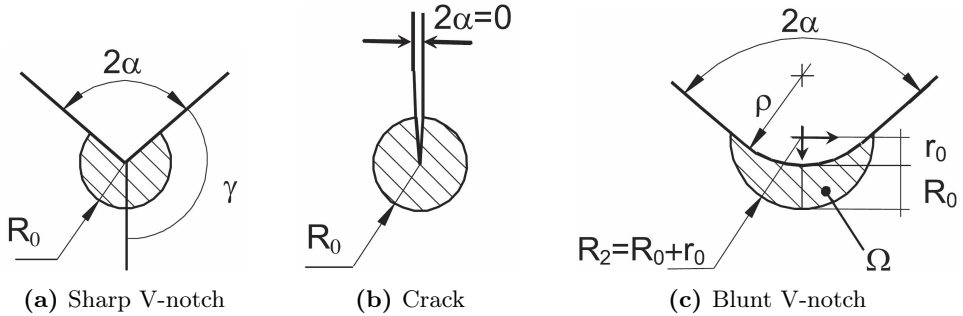
Figure 2.5: The control radius for different notches and cracks. (From Berto and Lazzarin (2009))

The control radius is applied in one of the three ways shown in figure 2.5. For sharp notches and and cracks, the R_0 is centered at the tip of the crack or notch (figure 2.5 (a) and (b)). For blunt notches, the center of the control radius is placed at a distance r_0 from the notch tip (figure 2.5 (c)). Calculation of the distance r_0 is shown in the previous section.

Calculation of the the control radius R_0 for a crack under plane strain conditions equation 2.11 is used (Aliha et al. (2017)). For a notch with an opening angle $2\alpha \neq 0$, other methods have been proposed to calculate the control radius (Lazzarin and Zambardi (2001)). However, according to Berto and Lazzarin (2009) it can be considered an acceptable engineering approximation to use the crack radius for different opening angles.

$$W_c = \frac{\sigma_{UTS}^2}{2E} \tag{2.10}$$

$$R_0 = \frac{(1+\nu)(5-8\nu)}{4\pi}\left(\frac{K_{IC}}{\sigma_{UTS}}\right)^2 \tag{2.11}$$

The radius R_2 shown in figure 2.5 (c) is obtained by adding R_0 and r_0. This is the distance from the center of the control radius to the edge of the crescent shape it forms around the notch tip. For blunt notches, this is the total control radius.

2.1.4 Connecting NSIF and SED

To be able to use ASED in the same way as NSIF's are used, some factors need to be in place. An area around the crack-tip needs to be defined to decide the density of the strain energy. Within a certain area of the crack-tip, the stress distribution is given by the NSIFS. By obtaining the ASED in this area, this value can in turn be used to calculate the NSIF's.

An expression to link the energy approach of ASED with NSIF's to create an energy-based failure criterion was proposed by Lazzarin and Zambardi (2001). The relation is presented in equation 2.12. By using this relation, the NSIF's of a notch or crack can be calculated indirectly through the ASED approach with the benefits that brings. For instance, mixed mode problems are made easier and a coarser mesh can be used which can drastically reduce the simulation time. Also, problems in regards to the different units on NSIF's from different notch opening angles are removed. It also takes into consideration higher order terms such as T-stress (Berto and Lazzarin (2014)). This will not be gone into detail in this thesis.

$$\overline{W}_1 = \frac{I_1}{4E\lambda_1(\pi - \alpha)}\left(\frac{K_1}{R_0^{1-\lambda_1}}\right)^2 \tag{2.12}$$

2.2 Finite Element Analysis

When calculating stresses in simple structures such as beams with constant cross-section, equilibrium laws can be used. In this case, the whole structure is looked at as one part. This method restricts the use to very simple geometries. FEA is useful when the geometry in question is of a more complicated nature. This is a numerical method for approximately solving a structure or other types of mathematical problems. The method divides geometries into several smaller parts

called finite elements. This can be done in either one, two or three dimensions. For each of the three dimensions, there are several different types of elements which can be used. However, in this case, only 2D analyses will be conducted, so only these types will be covered.
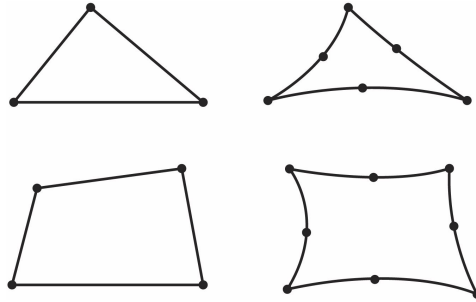
Figure 2.6: 2D element types. (From Dassault Systèmes Simulia (2014)).

For 2D analyses, there are two main types of elements, triangles and quadrilateral (squares). These can be either linear or quadratic. Linear elements have nodes only at the corners of the elements, while quadratic elements have nodes at the corners as well as on each midside. The main difference between the two being that linear elements use linear or first order interpolation of the degrees of freedom (DOF) between the nodes, while quadratic elements use second order interpolation between each node. In figure 2.6 both triangle (top) and quadrilateral (bottom) elements can be seen. On the left, linear elements are shown, while on the right, quadratic elements can be seen.

Generally in FEA, the use of finer mesh will give more accurate results. However, using fine mesh takes longer time to compute given the large number of nodes. It is therefore useful to know when it is necessary to use fine mesh, and when it is not. For instance, a large structure containing a stress riser such a hole can be meshed quite coarsely along most of the structure, but around the hole, it can be wise to decrease the size of the elements. This can decrease computation time considerably while maintaining the accuracy.

For some types of analyses, the accuracy of the results does not depend much on the element size. An example of this is when calculating the strain energy in a structure. The strain energy is a function of the nodal displacements within the structure, and does not require the displacements between nodes to be accurate. This is a fact which can be taken advantage of to decrease computational time and power.

2.3 Additive Manufacturing of PLA

AM has in the last decade become more and more popular. Its uses are many, such as rapid prototyping and creation of complex geometries. The use of AM will in the next couple of years only become more popular, as it becomes cheaper and better. There are more materials available for AM every day, and the material properties of the printed geometries keep getting better. In this section, some of today's AM methods used for printing polymer geometries are presented.

2.3.1 Additive Manufacturing

There are several ways of creating physical geometries through AM. However, each method restricts what materials can be used. the most used AM methods today according to Wang et al. (2017) are presented in the list below. In figure 2.7 the five different methods are shown.

1. Fused deposition modelling (FDM)

2. Selective laser sintering(SLS)

3. Powder bed and inkjet head 3D printing(3DP)

4. Stereolithography(SLA)

5. 3D plotting/direct-write

Fused Deposition Modelling
This method is the most common for polymers. It uses one or more filaments of thermoplastics. The filament is fed through a heated nozzle which softens the polymer. The nozzle then deposits the soft polymer onto a surface where one layer at a time is created for the geometry being printed.

Selective Laser Sintering
Selective laser sintering uses a powder bed. A roller then distributes the powder evenly onto a build surface. When the powder is distributed, a laser sinters the desirable shape of each layer by heating the substance. This whole process is repeated for each layer, until every layer has been created, one on top of the other to create a 3D geometry.

Powder Bed and Inkjet Head 3D Printing
This method is similar to the selective laser sintering. The main difference between these two methods is the binding method. Here, a liquid binder is distributed on top of each layer of powder, instead of laser sintering. The procedure of rolling new powder and binding is repeated for each layer.

Stereolithography
Stereolithography deviates from other methods by using a tank of photocurable resin. The print surface starts just beneath the surface of the resin. A laser then

cures the resin in the desired shape. The printing surface with the first layer of the 3D geometry then moves down a step so that the surface of the resin bath covers the previous cured layer. The laser then repeats the process for the next layer. This whole process is repeated until the geometry is finished.

3D Plotting/direct-write

3D plotting uses viscous material stored in a syringe. This material is extruded onto the print surface in a similar manner to FDM. The difference here, is that the material requires curing. This can be done by either using heat, UV light or mixing nozzles, depending on what material is being used.

2.3.2 PLA

Polyactide is a polymer created from biomass, and is therefore biodegradable. Several types of plant matter can be used, such as sugarcane, potatoes, tapioca roots, chips and cornstarch. PLA is relevant to use as a material in medical equipment where biodegradability is wanted (Ahmed and Susmel (2018)). As a material it is very close to plastics such as ABS. PLA is described as an aliphatic polyester which can withstand temperatures up to $110°C$ (Kariduraganavar et al. (2014)). It is soluble in most organic solvents, such as chlorinated solvents, benzene and acetonitrile. PLA is suitable for packaging of food items and goods for not too long periods. If left in nature, it will degrade to harmless natural compounds within a year. It is also used for medical equipment because of its biodegradability. If left inside the body, it can gradually degrade to give the body time to adapt to it not being there over a long time (Garlotta (2001)).

2.3.3 Anisotropy

Most of linear elastic fracture mechanics requires an isotropic nature of the material in question. Isotropy means that a material has the same strength in all directions. If a sphere is assumed, pulling the sphere in one direction with the force F should give the same result as pulling it in an arbitrary direction with the same force F. Examples of this are untreated cast metals and plastics.

Anisotropy describes a material which does not fulfill these criteria. Laminates and wood are typical examples of anisotropic materials. Most of today's AM methods involve building one layer at a time. To be able to create an isotropic material by this method, the adhesion between each layer has to be in such a manner that it does not affect the overall strength of the structure. Achieving this is very difficult.

When using FDM, the anisotropy is not just between the layers of each section. The adhesion between each single filament and the surrounding filaments as well as the angle in which they are printed come into play. In figure 2.8 two different samples can be seen. The sample in figure 2.8 (a) shows a sample where all filaments are printed longitudinal to the loading direction. This gives a fracture surface which is close to perpendicular to the loading direction. The specimen in figure 2.8 (b) has been printed with every other layer at a $45°$ and $−45°$ angle to the loading direction. This gives a fracture surface which creates a sawtooth pattern across the

(a) Fused deposition modelling

(b) Selective laser sintering

(c) Powder bed and inkjet head 3D printing

(d) Stereolithography

(e) 3D plotting/direct write
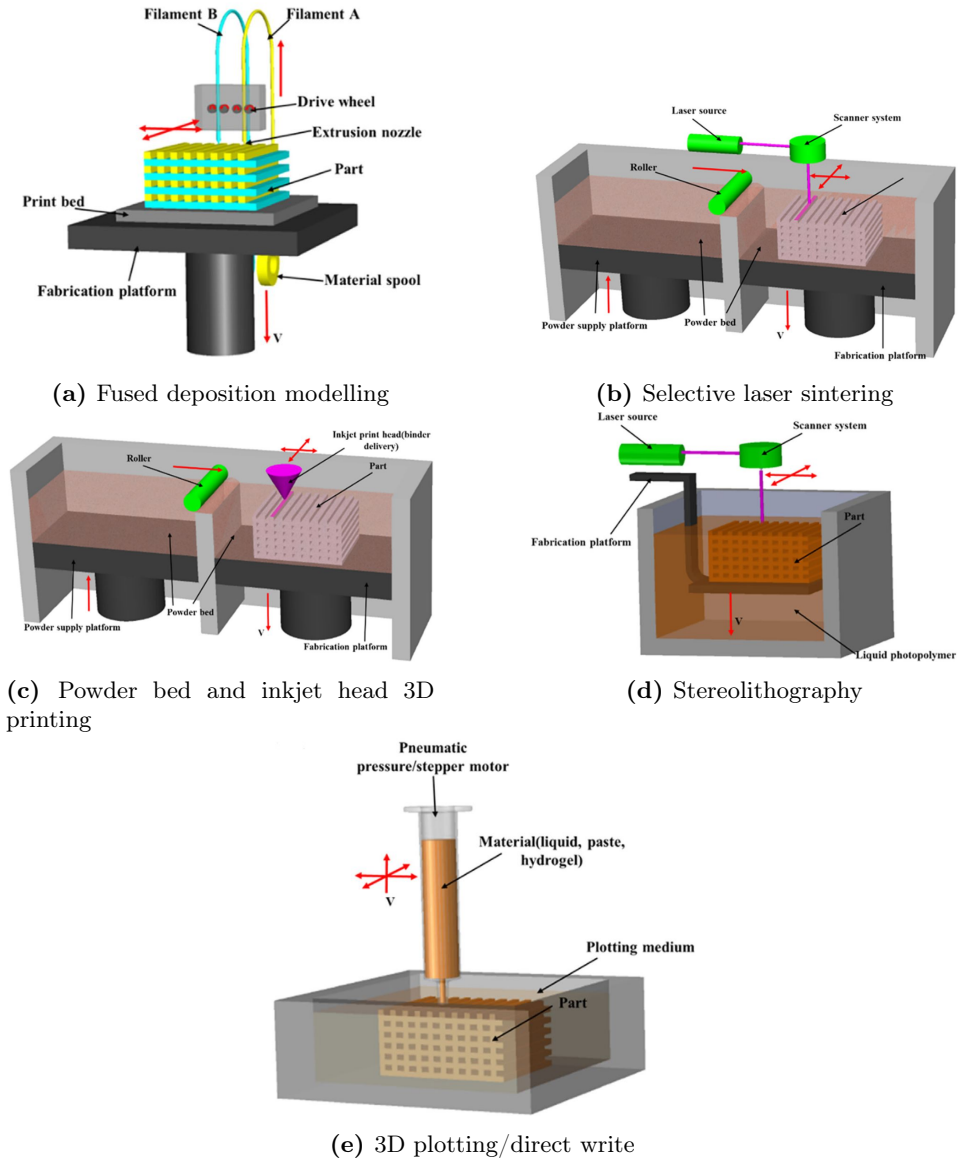
Figure 2.7: 5 different AM methods for polymers. (From Wang et al. (2017))

cross-section. From the SEM picture it is possible to see that almost every filament fails perpendicular to the longitudinal direction of the filament.
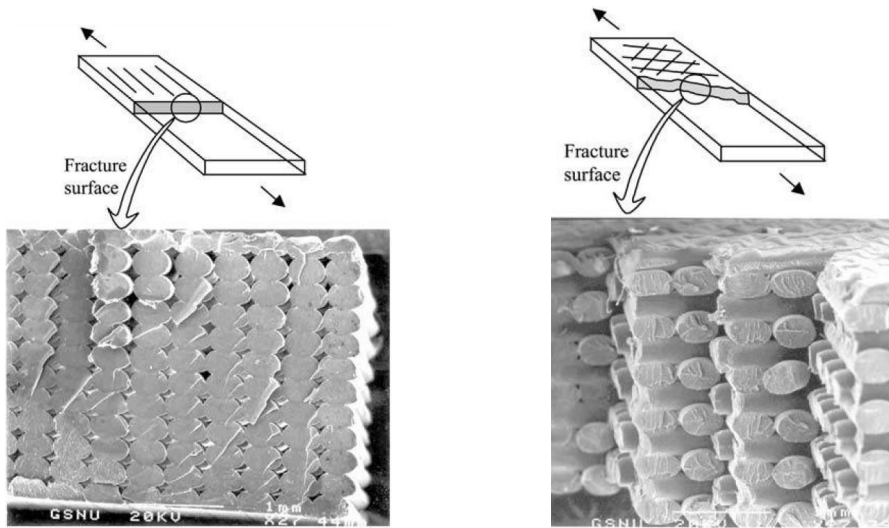
(a) Specimen printed with filaments longitudinal to loading direction.

(b) Specimen printed with every other layer 45° and −45° to loading direction.

Figure 2.8: Scanning electron microscope pictures of the fracture surface of two different FDM produced ABS samples. (From Ahn et al. (2002))

3 | Literature

This chapter covers some articles which were considered to be important in relation to the topic at hand. Each section summarizes one article. All the figures, tables and equations used in this chapter, are taken from the respective articles. The article in section 3.1 looks into using LEFM to asses the fracture load of AM PLA specimens. It covers everything from obtaining material properties, to testing, and comparing analytical results to actual test data. The testing work conducted in this paper lays the groundwork for the work being done in this thesis.

The articles in sections 3.2 and 3.3 cover ASED. They look at how it can be applied to both static and cyclic loading, as well as different types of notches and cracks. Mixed mode conditions are also covered, as well as different types of materials.

3.1 Application of LEFM to Additively Manufactured Specimens

The use of AM has in the later years become more and more popular. Thus, being able to understand and analyze structures made by such methods becomes increasingly important. In this paper, several different specimens have been printed using fused deposition modeling (FDM).

Due to the nature of AM, which can create very intricate and complex geometries, it is important to be able to understand the effect of notches in such specimens. A study into this was conducted by Ahmed and Susmel (2018). This was done by creating and testing a large variation of notched specimens printed in PLA. Both V and U notches, subjected to both tensile and 3-point bending regimes. The test results were then compared to analytical calculations using the theory of critical distance (TCD). The following section is a collection of the parts considered the most important from Ahmed and Susmel (2018).

3.1.1 The Theory of Critical Distance

The TCD is a collection of three different methods of determining the effective stress (σ_{eff}) in the vicinity of a crack or notch. The value is then compared to the ultimate tensile strength of the material. In short, the relation in equation 3.1 has to be fulfilled to avoid fracture according to the TCD. The three methods are all a function of the distance L which can be determined using equation 3.2, assuming brittle material properties ($\sigma_0 = \sigma_{UTS}$).

$$\sigma_{eff} < \sigma_0 \qquad (3.1)$$

$$L = \frac{1}{\pi}\left(\frac{K_{IC}}{\sigma_{UTS}}\right)^2 \qquad (3.2)$$

(a) Area method   (b) Line method   (c) Point method
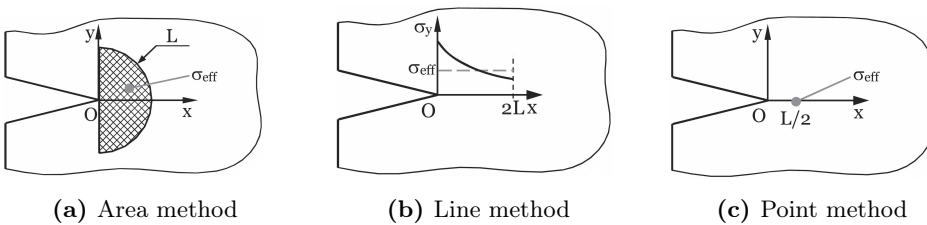
Figure 3.1: The local coordinate systems for the three methods of TCD. (From Ahmed and Susmel (2018))

Area method
The area method uses a semi-circle with its center at the crack-tip and a radius equal to L as shown in figure 3.1(a). The σ_{eff} in this case, is decided by integrating

across this area as a function of the principal stress in accordance with equation 3.3.

$$\sigma_{eff} = \frac{4}{\pi L^2} \int_0^{\pi/2} \int_0^L \sigma_1(\theta, r) \cdot r \cdot dr \cdot d\theta \tag{3.3}$$

Line method

The line method calculates the σ_{eff} by averaging the stress across the distance $2L$ along the notch bisector line as shown in figure 3.1(b). The integration formula is shown in equation 3.4, where σ_y is the stress perpendicular to the notch bisector line at any given point.

$$\sigma_{eff} = \frac{1}{2L} \int_0^{2L} \sigma_y(\theta = 0, r) \cdot dr \tag{3.4}$$

Point method

The point method states that the effective stress due to a crack is equal to the stress perpendicular to the crack bisector line at a distance $L/2$ from the crack tip. This is shown in figure 3.1(c). Calculating the effective stress is done using equation 3.5.

$$\sigma_{eff} = \sigma_y\left(\theta = 0, r = \frac{L}{2}\right) \tag{3.5}$$

3.1.2 Fabrication and Testing of the Specimens

To decide different material properties, several specimens were made for this purpose. These included a dog bone, a notched tensile specimen, as well as two CT specimens. However, only the dog bone and most relevant CT specimen will be included. The other two specimens can be seen in the reference article. The two specimens included in this report can be seen in figure 3.2.

(a) Dog bone specimen   **(b)** CT specimen
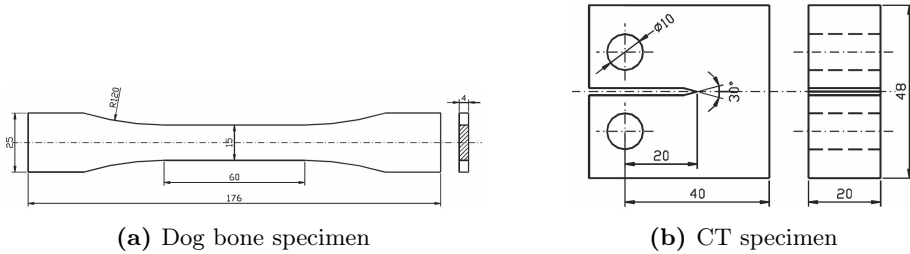
Figure 3.2: The two main specimens used for determining material properties. (From Ahmed and Susmel (2018))

The material properties to be decided by these two specimens are the Young's modulus (E) from the dog bone in figure 3.2(a), and the fracture toughness (K_{IC}) from the CT in figure 3.2(b).

However, FDM printing can give a lot of different material properties of samples by using different printing angles, shell thickness, nozzle diameter, print speed, material, and several other variables. To give some idea of how two of these factors, printing angle and shell thickness, affects this, several different variations of the two were tested in the dog bone samples. All variations are tested with three different samples to be able to identify irregularities in the test results.

The printing angle (θ_p) is the angle at which the specimens are laid onto the build plate (figure 3.3). The printer used in this case, builds every other layer perpendicular to the former. This means that for instance using $\theta_p = 45°$ means that every other layer is longitudinal and perpendicular to the loading direction of the specimen, $[0°, 90°]$. Five different printing angles were tested using the dog bones: $0°, 30°, 45°, 60°$ and $90°$.
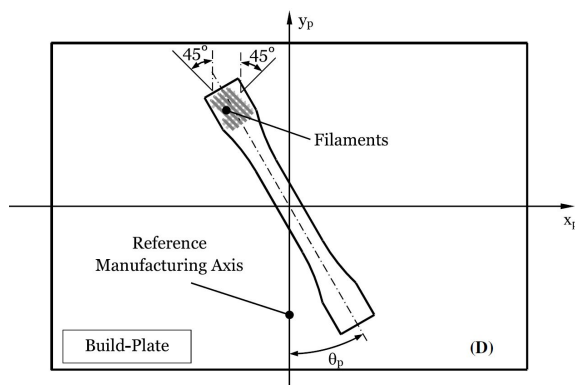
Figure 3.3: Definition of the printing angle θ_p. (From Ahmed and Susmel (2018))

When acquiring the fracture toughness from the CT samples, some lesson learned from the dog bone samples were taken into account. The samples printed using angles $0°$ and $90°$, as well as $30°$ and $60°$, gave very similar results. This resulted in that for all the next tests, only the angles $0°, 30°$ and $90°$ were used. Also, the shell thickness was set to $0.4mm$, which is equivalent to the nozzle diameter, for all samples. This was due to several factors. First, it is considered good practice to use only one filament width as the shell thickness when conducting material testing. Second, the resulting E, $\sigma_{0.2\%}$ and σ_{UTS} showed very little variation when changing the shell thickness. Third, when not including any shell thickness, a significant amount of stress risers, in the form of small indents, will be present. These stress risers are a large source of errors in testing, and are therefore unwanted. The shape factor used when calculating the fracture toughness was the one reported by Tada et al. (1973).

The notched samples from figure 3.4 were tested in the conditions mentioned above. The three printing angles were all tested three times for each specimen. This means that nine tests were run for each specimen type. The results from these tests were then compared to the predicted failure loads from TCD.

When using TCD to predict failure load of the specimens, the failure stress, σ_0
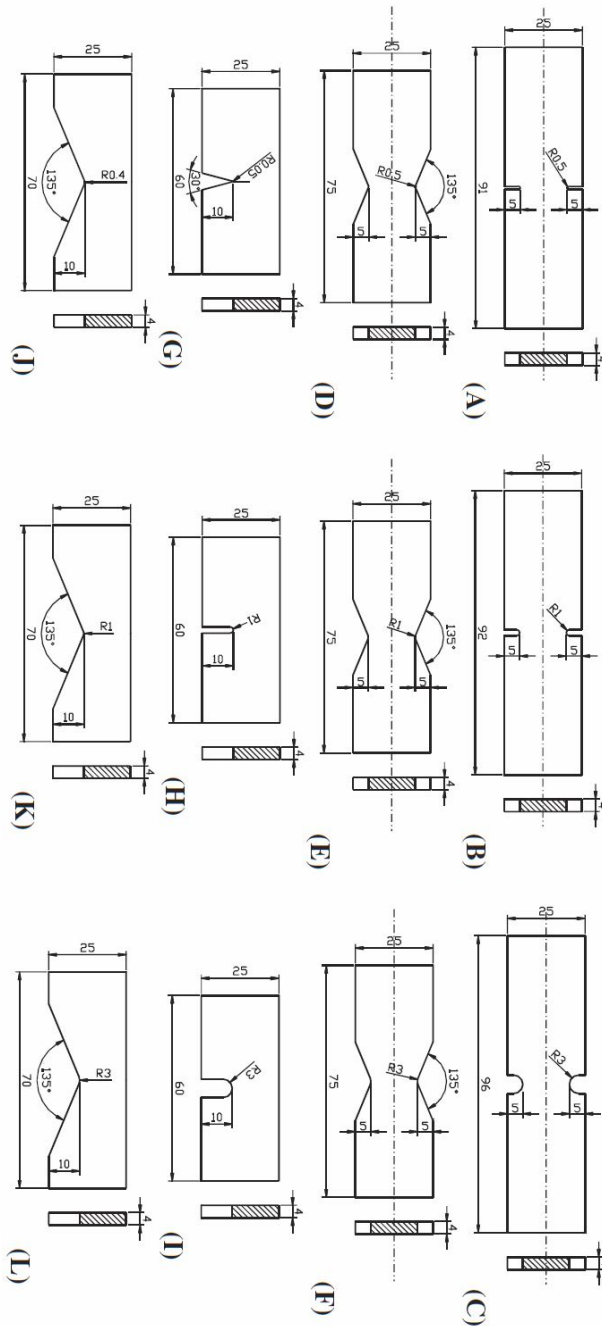
Figure 3.4: The 12 notched specimens being tested. (From Ahmed and Susmel (2018))
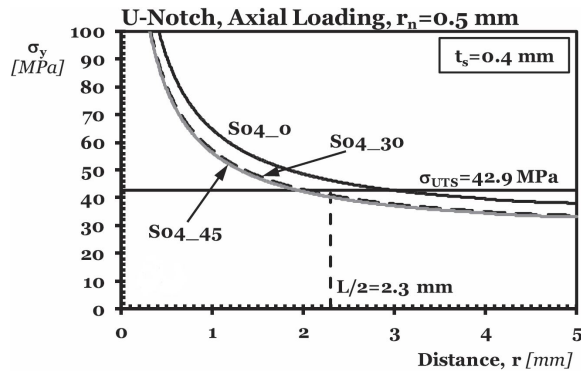
Figure 3.5: Stress vs distance curves for sample A. (From Ahmed and Susmel (2018))

was needed. A brittle material property is assumed for these situations, and this is the case with most of the additively manufactured PLA specimens. The stress strain curves from the testing gave a material strength very close to the UTS, as well as a typical brittle curve shape. It is therefore deemed safe to assume that $\sigma_0 = \sigma_{UTS}$. For the calculations conducted, a value for L from equation 3.2 was needed. Calculating L from this equation requires a fracture toughness for the material. The authors of the article did not deem the results from testing the CT specimens or a tensile specimens with crack-like notches accurate enough to use for the calculations.

Instead, an alternative method was used. The test results from specimen A from figure 3.4 were used to create three stress v distance curves (figure 3.5). One for each printing angle. This linear elastic stress field was then used to determine a value for L, using the point method definition (the stress at a distance $L/2$ from the notch tip is equal to the UTS). The point used, was an average of all three curves. This resulted in a value of $L = 4.6mm$. This method is also presented in Susmel and Taylor (2008).

Next, the three TCD criteria were applied to all the specimens, and compared to the experimental test results. The line method turned out to not be applicable in this case due to $(2L = 9.2mm)$ was larger than half the width of the test samples. However, both the point and the area method gave good results. The error in the graphs were calculated according to equation 3.6.

$$Error = \frac{\sigma_{eff} - \sigma_{UTS}}{\sigma_{UTS}} \tag{3.6}$$

The results, which can be seen in figure 3.6, give a fairly low percentage error. The peak errors for each criterion is at about 40%. However, most of the results are within an error of 20% which is considered well within the errors which one normally accepts for all LEFM.
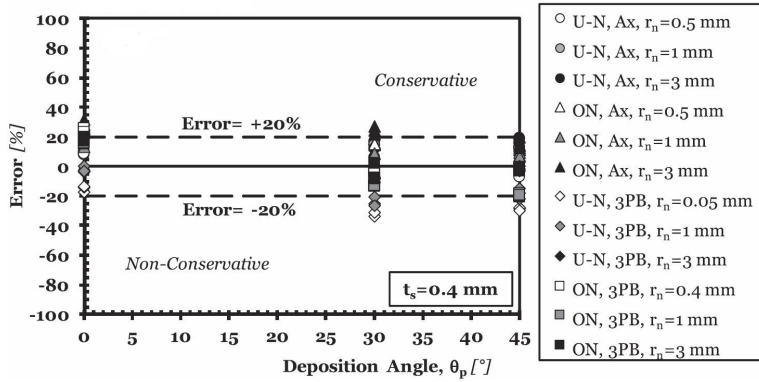
(a) Errors from using the point method.
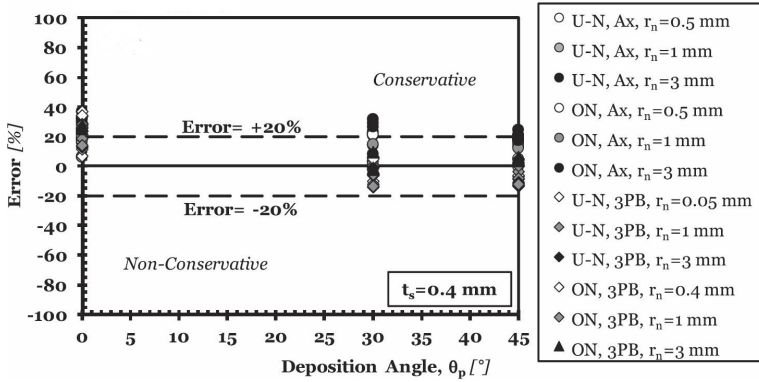
(b) Errors from using the area method.

Figure 3.6: The accuracy of the point and area method in determining the fracture load. (From Ahmed and Susmel (2018))

3.2 Application of the ASED Approach to Sharp and Blunt Notches

The use of averaged strain energy density over a control volume to indirectly calculate stress intensity factors in cracks and notches are explored in this section. The section is based on the work conducted by Lazzarin et al. (2010). When a control radius is small enough around a v-notch with ($\rho = 0$), the strain energy density can be written as a function of the first order terms of the asymptotic stress distributions. It is also shown that it is not dependent on sharp notches to be applicable. These values only depend on the notch stress intensity factors. This allows the practice of converting ASED values to NSIF values a posteriori. The advantage being that calculation of ASED is only to a small degree dependent on the mesh size. The first part of the article explores the effect of mesh size on ASED values, and the second looks more at using ASED to calculate NSIF's from different types of notches.

Using an ASED Approach to Welded Geometries Subjected to Tensile Loads

At first, two different geometries are studied. These have previously been analysed by Radaj et al. (2009). The Geometries can be seen in figure 3.7. The load was applied as a displacement u_0, to achieve a nominal stress of $\sigma_0 = 100MPa$. As control radius around the weld toe, a circle with a radius of $R_0 = 0.28$ is used. The ASED was calculated for both specimens from very fine meshes as well as coarse meshes. In figure 3.8 (a) and (b), two examples of the meshes used in the analyses can be seen. The results from geometry 1 can be seen in figure 3.9 and 3.10, while results from geometry 2 can be seen in figure 3.11. The reason for using different mesh sizes for the analyses was to be able to study the effect of the size. The hypothesis being that for energy based approaches using nodal displacements, the analyses are only dependent on mesh size to a small degree. All of these results are in agreement with the fact that using coarse meshes for conducting ASED analyses are well within the realms of what is acceptable. The largest deviations are at around 11%, which is only the case for two of the meshes tried for the notch. Both these meshes also have a very large size ratio between adjacent elements, which is a known factor which can give faulty results.
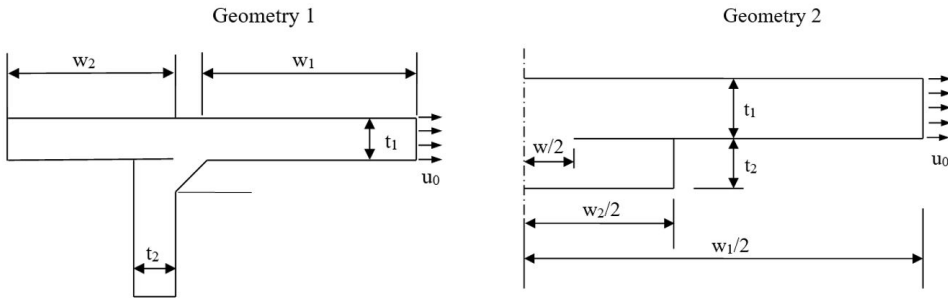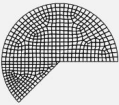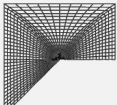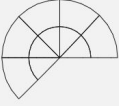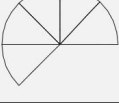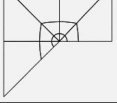
Figure 3.7: The two welded geometries analyzed. (From Lazzarin et al. (2010))

(a) Geometry 1
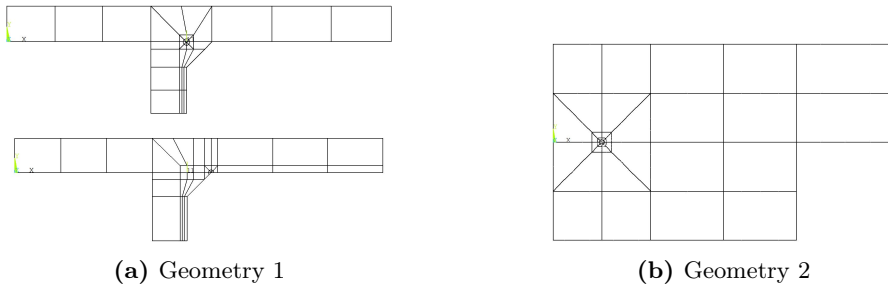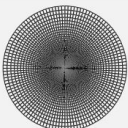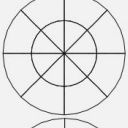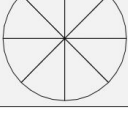
(b) Geometry 2

Figure 3.8: Examples of the meshes used on geometry 1 and 2. (From Lazzarin et al. (2010))

Figure 3.9: Results of ASED analysis for the weld root in geometry 1. (From Lazzarin et al. (2010))

Figure 3.10: Results of ASED analysis for the weld toe in geometry 1. (From Lazzarin et al. (2010))

Figure 3.11: Results of ASED analysis from geometry 2. (From Lazzarin et al. (2010))

ASED From Sharp V-notches

According to William's solution, the stress intensity factors for sharp V-notches in plane problems can be calculated with accuracy using equations 3.7 and 3.8 (Williams (1952)). For mode I and II cases, the local stress is proportional to $1/r^{1-\lambda_1}$ for mode I, and $1/r^{1-\lambda_2}$ for mode II. This fact is taken advantage of when

applying this to an energy-based approach.

$$K_1 = \sqrt{2\pi} \lim_{r \to 0^+} r^{1-\lambda_1} \sigma_{\theta\theta}(r, \theta = 0) \tag{3.7}$$

$$K_2 = \sqrt{2\pi} \lim_{r \to 0^+} r^{1-\lambda_2} \sigma_{r\theta}(r, \theta = 0) \tag{3.8}$$

A simple relation between the ASED and NSIF is given in equation 3.9, where e_1 and e_2 are dependent on the notch opening angle, Poisson's ratio and plane stress or plane strain conditions. This equation can be simplified for problems concerning only mode I or only mode II stress distribution. In these cases, one of the terms from the equation is equal to zero which removes the term, leaving an equation containing NSIF for one mode as well as the resultant ASED.

$$\overline{W} = \frac{e_1}{E}\left[\frac{K_1}{R_0^{1-\lambda_1}}\right]^2 + \frac{e_2}{E}\left[\frac{K_2}{R_0^{1-\lambda_2}}\right]^2 \tag{3.9}$$

When loading the sample in figure 3.12 as shown in the figure both mode I and II NSIF's appear in both the $2\alpha = 135°$ and $2\alpha = 45°$ corners. To be able to calculate the NSIF's when both mode I and II are present, the ASED over two control radii are necessary. Both have their center at the notch-tip, but different radius. Both the $2\alpha = 45°$ corners have stress distributions due to both mode I and II singular. This gives stresses proportional to $1/r^{0.495}$ for mode I and $1/r^{0.376}$ for mode II. Only the mode I stress field is singular for the $2\alpha = 135°$ corners, giving stresses proportional to $1/r^{0.326}$ for mode I, and $r^{0.302}$ for mode II.

In table 3.1 the results from the mixed mode analysis on a diamond notch can be seen. The difference gotten from using fine and coarse meshes are shown as deviation in percentage. For the corners with $2\alpha = 45°$, 16 and 8 elements have been used, with a difference of approximately 3% for both mode I and II. for the $2\alpha = 135°$ corners, 8 and 4 elements are used, with a difference of approximately 1% and 4% for mode I and II respectively.
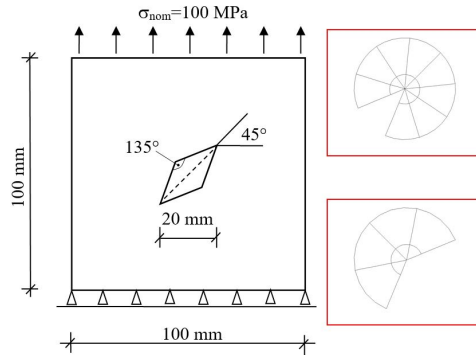
Figure 3.12: Diamond shaped notch giving mixed mode I and II. (From Lazzarin et al. (2010))

Table 3.1: Results from analyses on figure 3.12. K_1 in $MPa(mm)^{1-\lambda_1}$ and K_2 in $MPa(mm)^{1-\lambda_2}$. (From Lazzarin et al. (2010))

Mixed mode			Fine mesh		Coarse Mesh					
2α	λ_1	λ_2	K_1	K_2	Number (rad. 1)	Number (rad. 1)	K_1	K_2	$\Delta K_1[\%]$	$\Delta K_2[\%]$
45	0.505	0.624	355	325	8	16	366	315	-3.09	3.1
135	0.674	1.302	127	-97	4	8	128	-101	-0.78	4.1

ASED From Blunt U- and V-shaped Notches

The use of averaged SED over a control radius can also be used for blunt notches ($\rho > 0$). Equations 3.10 through 3.12 are valid for an infinite plate under remote uniaxial tensile stress, S (Kirsch (1896)). The equations use a polar coordinate system (r, θ), where $\theta = 0$ is the load direction. See figure 3.13.

$$\sigma_{rr} = \frac{S}{2}\left[1 + 3\left(\frac{a}{r}\right)^4 - 4\left(\frac{a}{r}\right)^2\right]cos2\theta + \frac{S}{2}\left[1 - \left(\frac{a}{r}\right)^2\right] \tag{3.10}$$

$$\sigma_{\theta\theta} = -\frac{S}{2}\left[1 + 3\left(\frac{a}{r}\right)^4\right]cos2\theta + \frac{S}{2}\left[1 + \left(\frac{a}{r}\right)^2\right] \tag{3.11}$$

$$\tau_{r\theta} = -\frac{S}{2}\left[1 - 3\left(\frac{a}{r}\right)^4 + 2\left(\frac{a}{r}\right)^2\right]sin2\theta \tag{3.12}$$

Maximum elastic stress is $\sigma_{\theta\theta} = 3S$ for $\theta = 90°$ and $r = R_1$. By creating a circle section with a center at $a/2$ from the edge of the hole, a crescent shape is formed on the outside of the hole. This gives two radii: R_1 and R_2. R_1 is constant, but R_2 varies according to equation 3.13. It is important not to mix this R_2 with the one from figure 2.5 (c), which is the distance from P to the outermost point of the crescent shape.
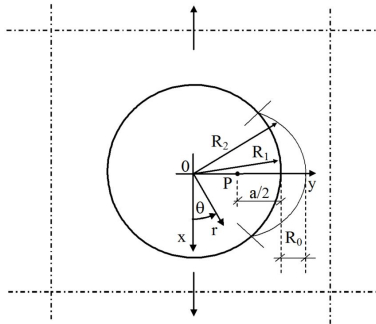
Figure 3.13: Plate with a radius of a, under tension. (From Lazzarin et al. (2010))

$$R_2(\theta) = \frac{1}{2}\left(asin\theta + \sqrt{4R_0^2 + 4aR_0 + a^2sin^2\theta}\right) \tag{3.13}$$

In equation 3.14 the formula for the angle $\overline{\theta}$ can be seen. This is the angle to the peak of the crescent control radius, which is used in equation 3.15.

$$\overline{\theta} = Arccos\left(1 - \frac{R_0}{a} - \frac{R_0^2}{a^2}\right) + \frac{\pi}{2} \tag{3.14}$$

The equation for calculating the strain energy density for an isotropic material under a linear elastic regime is shown in chapter 2 in equation 2.8. For plane strain conditions $\sigma_{zz} = \nu(\sigma_{rr} + \sigma_{00})$, and for for plane stress $\sigma_{zz} = 0$.

The values obtained from the previous equations, can be plotted into equation 3.15. This gives a new equation for the averaged strain energy density which can be seen in equation 3.16.

$$\overline{W}_1 = 2\left[\int_{+\pi/2}^{+\overline{\theta}} d\theta \int_{R_1}^{R_2} W(r,\theta)rdr\right]/A \tag{3.15}$$

σ_{max} substitutes the peak stress at the edge of the hole, which is $3S$. This correlation is only valid in infinite plates. However, values beneath 0.2 for R_0/a, give errors beneath 2%, given that σ_{max} substitutes $3S$.

$$\overline{W}_1 = \frac{\sigma_{max}^2}{2E} \cdot H(R_0/a) \tag{3.16}$$

The two models in figure 3.14 have been tested. First a stress analysis using fine mesh was conducted to identify σ_{max}. This was done to have a reference value for the peak stresses obtained from the ASED analysis. The ASED was then calculated using coarse mesh around the location of predicted peak stress. Equation 3.17 was then used to convert the ASED to stress. These values were then compared with the values obtained from the stress analysis conducted earlier. The results from these analyses can be seen in table 3.2. Also here, the max difference is around 5.5%.

$$\sigma_{max} = \sqrt{\frac{4E}{\pi} \cdot \frac{\overline{W}}{H}} \tag{3.17}$$

(a) Pure mode I.
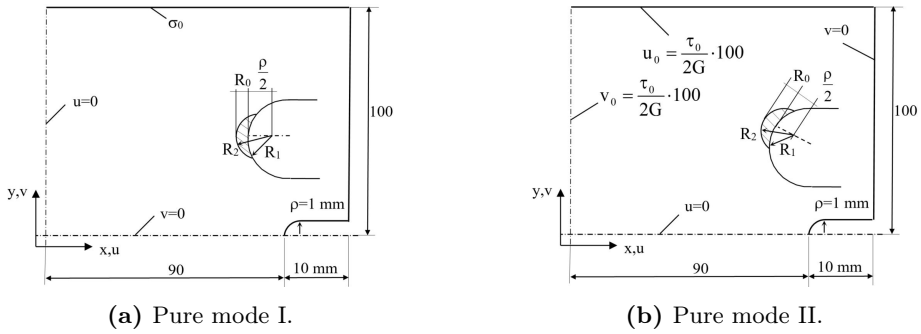
(b) Pure mode II.

Figure 3.14: Double symmetry applied to U-notch, under pure mode I (a) and pure mode II (b). (From Lazzarin et al. (2010))

Table 3.2: Results from pure mode I and II on U-shaped notches. (Data from Lazzarin et al. (2010))

| | Fine mesh | Parabolic FE (coarse mesh) | | | | |
	$\sigma_{max}[MPa]$	No. of elements (total)	No. of elements (radius)	$\overline{W}[MJ/m^3]$	$\sigma_{max}[MPa)]$	$\Delta[\%]$
Mode I, $2\alpha = 0°$	816	33	3	0.740	796	2.5
Mode II, $2\alpha = 0°$	880	34	4	1.186	830	5.6

3.3 Application of ASED to Predict Mixed Mode Problems

There are several ways of predicting the failure load of cracked specimens under mixed mode loading. Razavi et al. (2017) explores the feasibility of using the ASED criterion to accurately predict the failure load of cracked granite specimens under mixed mode I/II loading. The mixed loading was obtained from using a four point bending setup as shown in figure 3.15. Controlling the mixity of the modes is done by changing the relation between L_1, L_2, L_3, and L_4 as well as the relation a/W. This has earlier been shown by Ayatollahi and Aliha (2011).
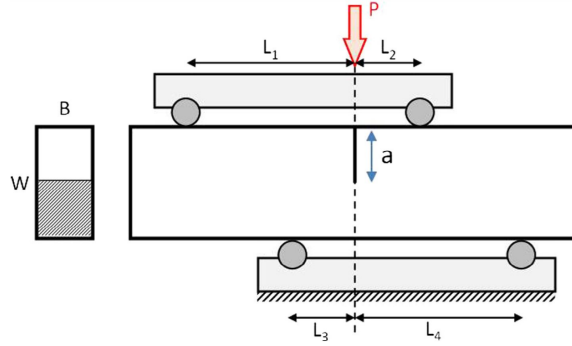
Figure 3.15: A schematic of the four point bending setup (AFPB). (From Razavi et al. (2017))

For any mixed mode conditions for the AFPB, equations 3.18 and 3.19 can be used to calculate K_I and K_{II}. Y_I and Y_{II} are geometry factors for mode I and II. They depend on L_1, L_2, L_3 and L_4 and the relation a/W, and are computed using finite element analyses. The exact values can be found in the article in question.

$$K_I = \frac{P\sqrt{\pi a}Y_I}{BWL_1}(L_1 - L_3) \tag{3.18}$$

$$K_{II} = \frac{P\sqrt{\pi a}Y_{II}}{BWL_1}(L_1 - L_3) \tag{3.19}$$

A factor M_e is used to describe the load mixity in a crack. This is calculated using equation 3.20. This factor ranges from 1 (pure mode I) to 0 (pure mode II).

$$M_e = \frac{2}{\pi}\arctan\left(\frac{K_I}{K_{II}}\right) \tag{3.20}$$

The calculation of ASED has been covered extensively in previous sections in this thesis, and will therefore not be covered again. The formula for calculating R_0 can be seen in equation 2.11 in section 2.1.3.

The method used in this article to decide the fracture load of each case has its basis on using a critical SED (W_c). The square root of the relation between the

critical SED and the averaged SED equals the relation between the fracture load and applied load as shown in equation 3.21. Calculating the critical SED is done as shown in equation 2.10 from section 2.1.3.

$$P_{th}/P = \sqrt{W_c/\overline{W}} \tag{3.21}$$

The method described above was used to run FE analysis using the ASED approach to determine the failure load of several granite specimens subjected to different mixed mode load cases. Cases of pure mode I and II were also tested. The mixity of the loads was varied from pure mode I to pure mode II, including several values of M_e in between. The results can be seen in figure 3.16. This figure clearly shows a good correlation between the ASED approach and the experimental values.
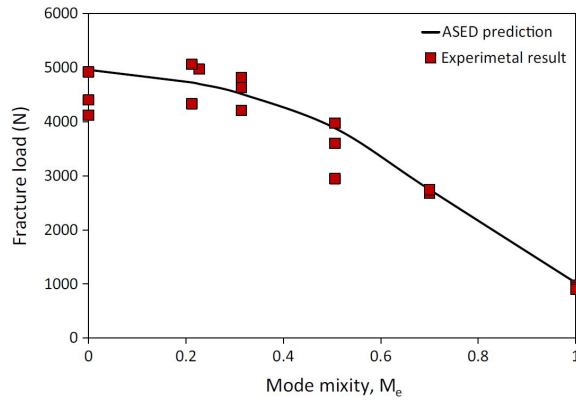
Figure 3.16: Results of ASED analysis compared to experimental results. (From Razavi et al. (2017))

4 | Analysis

4.1 Setup

The goal of these analyses is to check if it is possible to accurately predict the failure load of AM specimens of PLA using FEA in a linear elastic regime. There are several issues, such as anisotropy and material uncertainty which makes the analyses difficult. However, the goal is not to model the anisotropy as accurately as possible. It is to see if it is possible to simplify the structures, and assume isotropy and still get satisfactory results.

The work conducted in this thesis is based on the work done by Ahmed and Susmel (2018) in testing a large variety of notched AM PLA specimens under uniaxial loading and 3 point bending regimes. This work has been summarized in section 3.1.

There were mainly two different types of analyses conducted. The calculation of ASED withing a control radius and calculation of NSIF's around the different notches. The main thing separating the setup of these analyses is the mesh. Calculating the ASED using FEA does not require fine mesh which is shown by Lazzarin et al. (2010) for sharp notches, and also tested later in this thesis for blunt notches. For this reason, a coarser mesh is used for the ASED analyses than for the NSIF analyses. Apart from this fact, both analyses have the same setup.

The ASED analyses were run averaging the results from each printing angle respectively (3 samples for each printing angle), and running analyses simulating the material properties for each printing angle.

The analyses conducted:

1. Mesh sensitivity for ASED analyses

2. Required mesh for accurate NSIF's

3. Failure load using ASED approach

4. Failure load using NSIF approach

4.1.1 Material Properties

Given the anisotropic nature of the 3D printed specimens, some simplifications were conducted. The test results obtained from Ahmed and Susmel (2018) give the basis for calculating the modified material properties. The results from the tensile tests conducted on the dog bone sample shown in figure 3.2(a), are used to average a value for the Young's modulus as well as the UTS.

Three different shell thicknesses were used. However, the article chose to only use a shell thickness of $0.4mm$ for the notched samples, and therefore only the values obtained for the dog bone with the same shell thickness is used. Also, the dog bone samples were printed with five different printing angles ($0°, 30°, 45°, 60°$ and $90°$), but the notched samples were only printed using the three first angles. This was due the fact that printing angles $0°$ and $90°$ as well as $30°$ and $60°$ gave very similar results.

The difference in these values meant that it would be natural to calculate different material properties for each printing angle. This was done by averaging all three specimens for each case. The fracture toughness was calculated from the test results on the CT specimens, and the same procedure of averaging the three test results for each case was done. The Poisson's ratio was obtained from literature (Torres et al. (2015)). This Poisson's ratio is for molded PLA which is the closest it was possible to get without conducting experiments. The values obtained for each printing angle can be seen in table 4.1.

Table 4.1: The material properties used for each printing angle.

Printing angle [°]	Youngs modulus [MPa]	Ultimate tensile strength [MPa]	Fracture toughness [$MPa\sqrt{m}$]	Poissons ratio [-]
0	3235.0	42.7	4.6	0.36
30	3314.3	40.9	4.0	0.36
45	3372.0	42.5	4.2	0.36

4.1.2 Model

Preparing the models for analyses required several steps. All analyses were conducted in 2D to simplify the analysis. This meant that the geometries from figure 3.4 were modeled as specimen A, which can be seen in figure 4.1. A thickness was then added to the surface geometry. This thickness was averaged from the previously conducted tests. Next, the surface was partitioned to be able to extract the ASED from within the control radius. This is explained in more detail in section 4.1.5. This can be seen in the same figure.

Calculating the control radii for the analyses was done in the same way as described by Razavi et al. (2017). Equation 2.11 from section 2.1.3 was used. This equation requires the Poisson's ratio, fracture toughness, and UTS. This means that there are different control radii for each printing angle. The same goes for the critical SED. The equation used to calculate is dependent on UTS and Young's modulus as shown in 2.10. These values can be seen in table 4.2.

Since all the specimens being tested are of a blunt nature, the center of the control radius also has to be calculated. This is done according to the equation
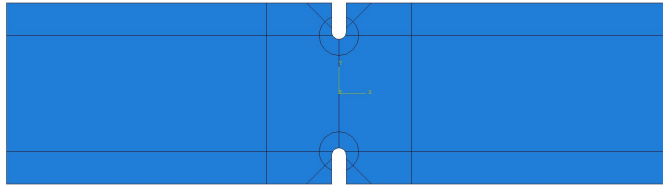
Figure 4.1: The partitioned geometry of specimen 3B.

Table 4.2: The values used for control radius and critical SED.

Printing angle [°]	R_0 [mm]	W_c [mJ/mm^3]
0	2.67	0.28
30	2.16	0.25
45	2.24	0.27

presented in figure 2.4. For the notches with opening angles $2\alpha = 0°$, this simply gives $r_0 = \rho/2$. For the specimens with other opening angles, however, the value has to be calculated specifically for each case. In table 4.3 the obtained values are presented.

The opening angle 2α is given in radians. There are only two opening angles in this case which are not equal to zero, which are $2\alpha = 30° \rightarrow 0.524rad$ and $2\alpha = 135° \rightarrow 2.356rad$.

Table 4.3: The values calculated for r_0 for every case.

2α [rad]	$\rho[mm]$	$r_0[mm]$
0.524	0.05	0.023
2.356	0.4	0.080
2.356	0.5	0.100
2.356	1	0.200
2.356	3	0.600

The values obtained for R_0 and r_0 are added together to give the radius R_2 which is the distance from the center of the control radius to the outermost point of the crescent point of the control radius. A depiction of R_2 is given in figure 2.5 (c).

4.1.3   Mesh

As previously shown by Lazzarin et al. (2010), calculating the ASED from within a control radius is not dependent on fine mesh. However, the mesh dependency conducted in these analyses were done for cracks and sharp V-notches. In the cases being considered here, all specimens are either blunt U- or V-notches. For that reason, it was considered reasonable to conduct a comparison with the models in question. This was done by using three different versions of specimen A, with

the same printing angle. For each version, the number of FE within the control radius was increased. The results from all three were then compared to the result from the analyses conducted using coarse mesh.

(a) Coarse mesh for ASED analysis.

(b) Control radius, coarse mesh.

(c) Fine mesh for NSIF analysis.

(d) Control radius, fine mesh
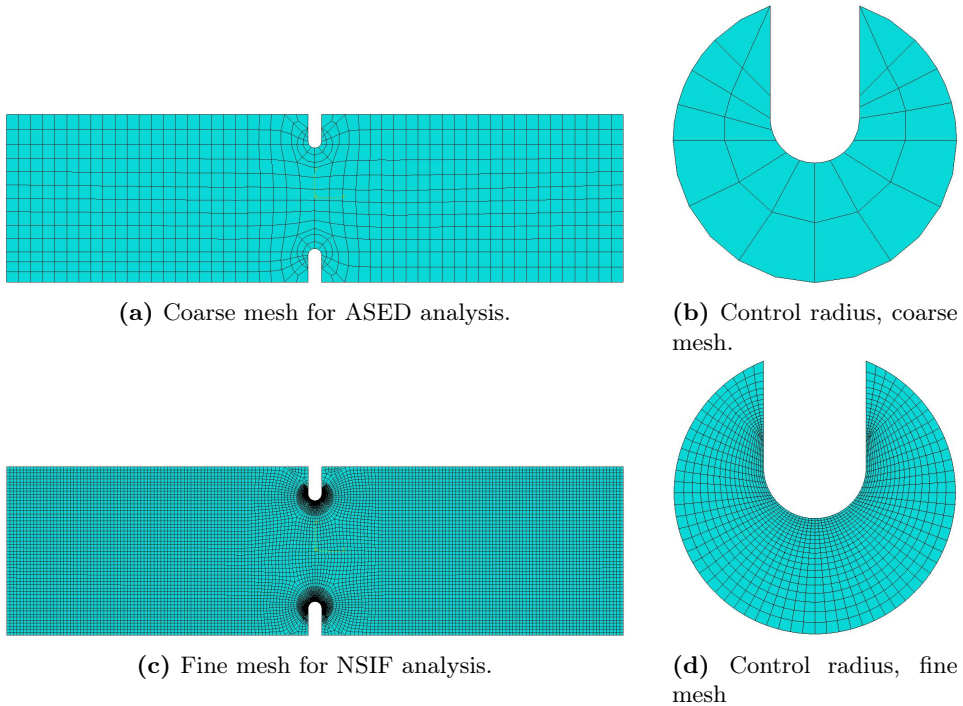
Figure 4.2: Specimen 3B with coarse mesh, whole model in figure (a) and control radius in (b). Fine mesh, whole model in figure (c) mesh and control radius in figure (b).

An analysis to obtain the NSIF's for all of the notches in question was also conducted. To be confident that the values were to be trusted, a mesh dependency analysis was also conducted here. In this case, it was done by finding NSIF's using a very coarse mesh. Then, the mesh size was decreased stage by stage to see how it affected the resultant NSIFS's.

For all analyses, quadratic mesh, under plane strain conditions was used.

4.1.4 Constraints and Loads

The specimens being tested were applied loads and boundary conditions to simulate the real conditions under experimental testing as best as possible. This is important because the results from the simulations are to be compared to the test results. All specimens were applied a unit load, which means a load that is equal to one. In this case $1N$. The reason for applying a unit load is so that when the formulation from equation 3.21 is used, the fracture load equals the root of the critical SED divided by resulting ASED.

There are two main types of specimens being tested: uniaxial tension (figure 4.3 (a)) and 3 point bending (figure 4.3 (b)) specimens. Both are to be applied a unit load. For the 3PB specimens, this is easily done by applying a concentrated force at the midpoint of the top of the specimen equal to one.

The BC's for the 3PB specimens are of a displacement/rotation type. The constraints are placed $5mm$ from the corner on each side. On the left-hand side, displacement in both x- and y-direction is constrained, while on the right, only displacement in the y-direction is constrained.
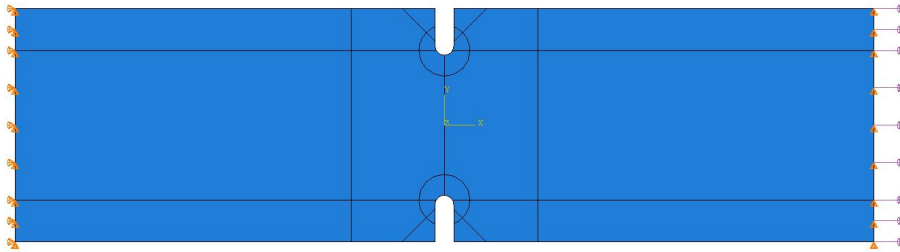
(a) Axial specimens.
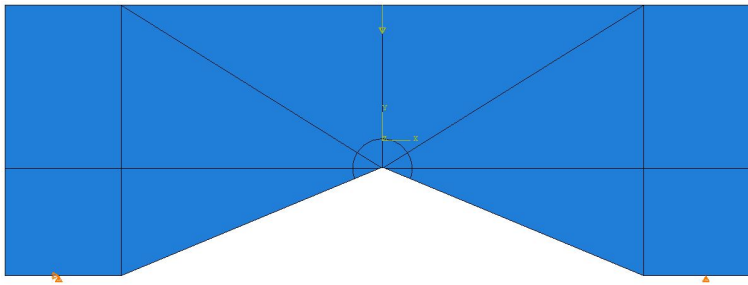
(b) 3 point bending specimens.

Figure 4.3: The loads and BC's as they are applied to both axial and 3PB specimens.

From the listed measurements of all the specimens tested from Ahmed and Susmel (2018), the thickness of the specimens are not all equal. They vary from $4.1mm$ to $4.3mm$. This means that to be able to apply a load equal to one across the cross-section, the thickness of the sample needs to be taken into consideration. To apply a unit load to the different cross sections depending on the thickness, the formulation of pressure is used ($P = F/A$). In the list below, the applied pressure to the end surface for each case can be seen. The pressure is applied with a negative unit to achieve a tensile and not compressive regime.

1. $t = 4.1mm \rightarrow P = 0.0098N/mm^2$

2. $t = 4.2mm \rightarrow P = 0.0095N/mm^2$

3. $t = 4.3mm \rightarrow P = 0.0093N/mm^2$

The axial specimens were constrained on the left-hand side from displacement in both x- and y-direction along the whole end surface. On the right-hand side, only displacement in the y-direction is constrained. This method turned out to give the best equal distribution on both sides of the bisector line.

4.1.5 Outputs and Calculations

To calculate the ASED inside the control radius of the specimens in question, two outputs are needed from the FEA software. The ASED is simply the strain energy per volume unit. To be able to request outputs from within a certain area, the partitioned control radius is selected as a "set". This set can in turn be selected as a "display group" in the analysis results. The outputs "ELSE" for element strain energy and "EVOL", which is the element volume, is requested. Using equation 4.1, the ASED within the control radius can be calculated. This process is in principle the same if done in 2D or 3D models.

$$ASED = \frac{ELSE}{EVOL} \tag{4.1}$$

Once the ASED values are obtained, the relation between loads and resultant ASED values, presented in equation 3.21 in section 3.1, are used to calculate a predicted fracture load.

The calculation of NSIF's are a little more complicated. The same models are used as for ASED analyses, except the mesh size is decreased considerably. The NSIF's are not affected by the printing angle, which means that only one NSIF is needed for each specimen type. The K-values, in this case, only K_I values because of only mode I problems, are plotted using equation 2.7, presented in section 2.1.2. It is plotted using K_I values as a function of the distance from the center of R_2 on a logarithmic scale.

The values obtained for the NSIF's are converted to ASED a posteriori using two different formulations, both presented earlier in this thesis. The first NSIF's are converted to ASED using equation 3.9. This is the simplest of the formulations and is mainly for sharp notches with $2\alpha = 0$. The second NSIF's are converted using equation 2.12. These values are expected to be a little more accurate considering the fact that more factors are taken into consideration in the calculations. The ASED values obtained from these two calculations are then used to calculate a fracture load for each NSIF for each specimen and printing angle, using the same method as for the direct ASED calculations. These values are then compared to the averaged fracture load obtained from experiments. The fracture loads for the two NSIF's are named P_{NSIF1} and P_{NSIF2} respectively in the results section.

4.2 Results

The results from all the analyses and comparisons of the analytical and experimental results are presented in this section. The specimens being tested are all presented in figure 3.4 with labels A through L. In the graphs and tables they are also referred to by their geometrical properties as well as how they are tested. These factors are notch type, test type, and notch radius. The abbreviations are as follows:

- U = U-notch

- V = V-notch

- Ax = uniaxial/tensile load

- 3PB = 3 point bending

- r = notch radius

4.2.1 Mesh Sensitivity for SED Analyses

The first analyses that were conducted were to verify the mesh independence of the ASED analyses. The results from these tests can be seen in table 4.4. Three tests were run with decreasing mesh size for each step. The predicted fracture load from the different meshes are all compared to the result from the coarse mesh. The results give a practically non-existent difference. All three mesh sizes deviate from the coarse mesh with about 0.04%. These results give clear indications that a coarse mesh can be used for all ASED analyses without any risk of giving inaccurate results.

Table 4.4: Results from mesh sensitivity analysis for ASED calculations for specimen A with $0°$ printing angle.

	Fine mesh		Coarse mesh		
Specimen	No. FE in r_c	Pred. fracture load [N]	No. FE in r_c	Pred. fracture load [N]	Deviation [%]
1	1151	3168.3	64	3169.7	0.04
2	2936	3168.3	-	-	0.04
3	11259	3168.3	-	-	0.04

4.2.2 Mesh Sensitivity for NSIF Analyses

A mesh sensitivity analysis was conducted for the NSIF analyses as well. The size of the mesh is measured along the shortest edge of the element, perpendicular to the notch depth. Seven different mesh sizes were tested, ranging from $0.016mm$ to $0.174mm$. The results from each analysis is plotted in the graph in figure 4.4, with K_I as a function of the mesh size. The last point, with the coarsest mesh, give unsatisfactory results, but all the other points have very small percentage deviations. However, it was chosen to use a mesh size of approximately $0.05mm$ for all models to be certain the results were correct.
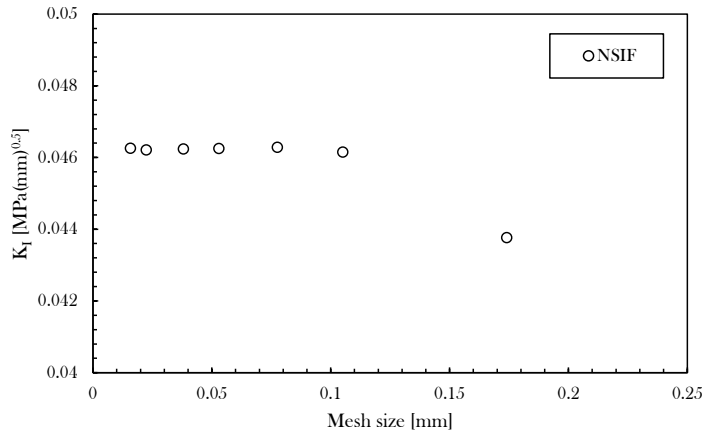
Figure 4.4: Result from mesh sensitivity analysis for NSIF.

4.2.3 Results from ASED analyses

The results from the ASED analyses are presented in this section. Each numerical result is individually compared to all three experimental result for each printing angle. They are presented in both table and graph form. It is presented in this manner separated for specimen type and printing angle to best be able to compare the results and show how much the results deviate from the experimental results. The "ELSE" and "EVOL" and resulting ASED values are presnted in table 6.1, located in the appendix.

ASED presented in table 4.5

In table 4.5 the results from the ASED analyses are presented in whole. Here, the three experimental results are presented and compared to the analytical results obtained from the ASED analyses. The experimental results are presented in the columns P_{exp1}, P_{exp2}, and P_{exp3}. The results from the ASED analyses are presented in the column P_{ASED}. In the columns Δ_1, Δ_2, and Δ_3 the deviations from the experimental results are presented respectively compared to the ASED result. The ASED results are compared to the experimental results using equation 4.2. This means that a positive deviation value, indicates an ASED result higher than the experimental result, being a non-conservative estimate. A negative value however, indicates the opposite, thus giving a conservative result.

$$\Delta = \frac{P_{exp} - P_{ASED}}{P_{exp}} \cdot 100 \tag{4.2}$$

From the results presented in the table, it is clear the U-notched specimens subjected to axial loading give the smallest deviations from the experimental results. A noticeable trend is also that the specimens with the smaller notch radius tend to have a better accuracy in terms of the experimental results compared to the analytical result. However, the V-notched 3 point bending specimens generally gave a bad accuracy. The worst accuracies are the ones for specimen J, with printing angle of 0°. All the experimental results are consistently around 40 % larger than the analytical results. It is also noticeable that the case of extra large deviations for 0° printing angles is a case for all of the different 3PB specimens. Both V- and U-notched.

Table 4.5: Details of the experimental data from Ahmed and Susmel (2018) compared to the results from using ASED criterion.

Specimen	Print angle [%]	$P_{exp1}[N]$	$P_{exp2}[N]$	$P_{exp3}[N]$	$P_{ASED}[N]$	$\Delta_1[\%]$	$\Delta_2[\%]$	$\Delta_3[\%]$
A - U, Ax, r=0.5mm	0	3234	3212	3218	3168	- 2	- 1	- 2
	30	2861	2815	2824	2774	- 3	- 1	- 2
	45	2777	2861	2713	2951	6	3	9
B - U, Ax, r=1mm	0	3355	3311	3327	3151	- 6	- 5	- 5
	30	3274	3262	3260	2757	- 16	- 15	- 15
	45	3206	3182	3174	2932	- 9	- 8	- 8
C - U, Ax, r=3mm	0	3330	3307	3294	3015	- 9	- 9	- 8
	30	2986	2706	3099	2610	- 13	- 4	- 16
	45	3179	3230	3763	2785	- 12	- 14	- 26
D - V, Ax, r=0.5mm	0	3302	3329	3325	2520	- 24	- 24	- 24
	30	3057	3108	3068	2291	- 25	- 26	- 25
	45	2858	3015	2960	2426	- 15	- 20	- 18
E - V, Ax, r=1mm	0	2670	3031	2669	2686	1	- 11	1
	30	2543	2889	2472	2334	- 8	- 19	- 6
	45	2939	2893	2825	2474	- 16	- 14	- 12
F - V, Ax, r=3mm	0	3195	3297	3216	2517	- 21	- 24	- 22
	30	3142	3195	3069	2263	- 28	- 29	- 26
	45	2826	2872	2997	2397	- 15	- 17	- 20
G - V, 3PB, r=0.05mm	0	1009	1049	1063	878	- 13	- 16	- 17
	30	810	-	847	747	- 8		- 12
	45	879	884	862	799	- 9	- 10	- 7
H - U, 3PB, r=1mm	0	1096	1050	1054	916	- 16	- 13	- 13
	30	813	865	803	779	- 4	- 10	- 3
	45	895	926	850	833	- 7	- 10	- 2
I - U, 3PB, r=3mm	0	1144	1131	1134	854	- 25	- 24	- 25
	30	875	873	874	717	- 18	- 18	- 18
	45	923	930	-	769	- 17	- 17	
J - V, 3PB, r=0.4mm	0	990	1015	996	597	- 40	- 41	- 40
	30	701	786	776	521	- 26	- 34	- 33
	45	660	640	647	555	- 16	- 13	- 14
K - V, 3PB, r=1mm	0	919	939	924	596	- 35	- 37	- 35
	30	696	690	693	520	- 25	- 25	- 25
	45	649	636	641	554	- 15	- 13	- 14
L - V, 3PB, r=3mm	0	887	902	907	578	- 35	- 36	- 36
	30	773	692	701	506	- 35	- 27	- 28
	45	753	744	734	538	- 29	- 28	- 27

ASED presented in graphs

The results from the ASED analyses are also presented in graphs shown figures 4.5 through 4.8, as well as figure 4.9. The results are presented as $(\overline{W}/W_c)^{0.5}$, where $\overline{W}$ is the obtained ASED from analyses, and W_c is the critical ASED from equation 2.10. The relation is presented in section 3.3, equation 3.21. By using this relation to present the results, the plots give a percentage deviation. For instance, a value of 1.2 for $(\overline{W}/W_c)^{0.5}$ means that the numerical result was 20% higher than the experimental result. Which in turn can be described as a non-conservative result, whilst a number below 1, is considered a conservative result. The results in figures 4.5 through 4.8 the analytical results are compared to each of the individual test results from all three of the experimental tests conducted on each sample. In figure 4.9 the analytical results are compared to the average from the three experimental result to be able to fit all results in one graph.

Figure 4.5 contains the results for samples A through C. They show a clear trend of increasing the uncertainty as the printing angle is increased up to 45°. For a printing angle of 0°, all three specimens have results which indicate a very good correlation between the analytical and experimental results. This is also the case for the samples printed at 30°, to some extent, although some of the results are around a value of 0.85. These values are well within what is considered acceptable, but they do show some deviation. The samples printed at 45° are spread over a larger area. All the samples with the smallest notch radius ($r = 0.5mm$), give non-conservative results. This can be confirmed as well by table 4.5. Although the results are spread out over a larger area, the mean value of these results are about the same as for the other two printing angles.
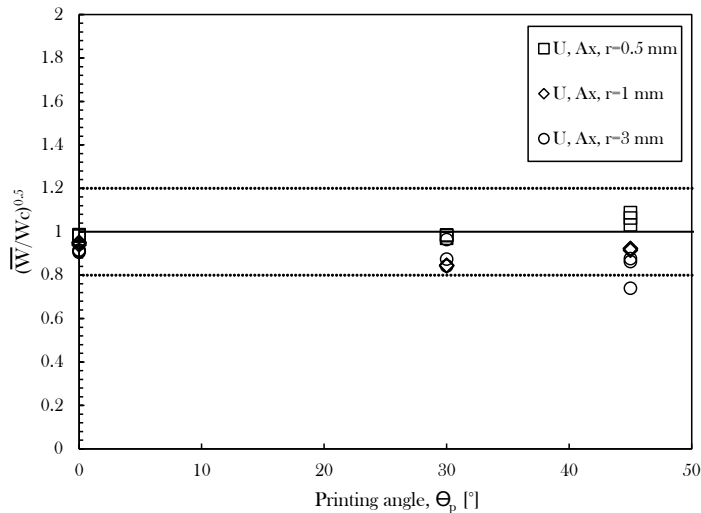
Figure 4.5: Results specimens A, B, and C.

Figure 4.6 contains the results from the ASED analyses conducted on specimens D, E and F. The specimens printed at an angle of 0° with a notch radius of $r = 1mm$ give the best results. Two of the test results have the same value, which is just above 1, while one is a bit lower at about 0.9. The rest of the tested specimens with the same printing angle are consistently at around 0.8.

When it comes to the specimens printed at an angle of 30°, much of the same as for 0° printing angle specimens can be said. The plots look very much alike, and the same specimen geometries have more or less the same values in the graph. The specimens printed at 45° angle, have remarkably consistent results. All of the plots have values which differ from around 0.8 to 0.9 in values. This can also be confirmed by looking at the values from table 4.5. From this table, it can be seen that the percentage deviation between the analytical and experimental results differ from about -12% to -20%.
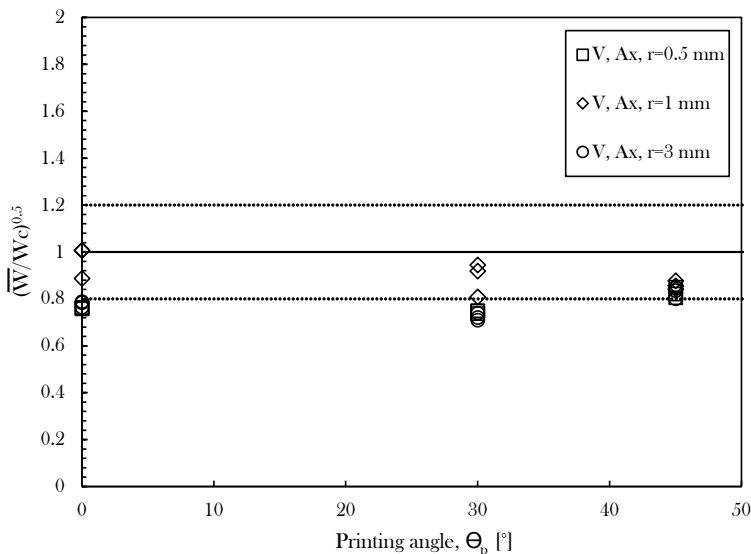
Figure 4.6: Results specimens D, E, and F.

The results presented in figure 4.7 are those obtained from the ASED analyses conducted on specimens H and I. It was decided to present the results from specimen G along with the other V notched 3PB specimens, instead of with the U-notched 3PB specimens, because of the geometry similarities. The two specimens H and I give results which are very consistent. For all printing angles, the smallest notch radius gave results closest to 1. The larger notch radius specimens though, were the most consistent specimens of all, although all had a $(\overline{W}/W_c)^{0.5}$-value of around 0.8. From table 4.5 there was only one specimen tested which did not have the same percentage deviation as the others, and this was a deviation of only 1 percentage point.
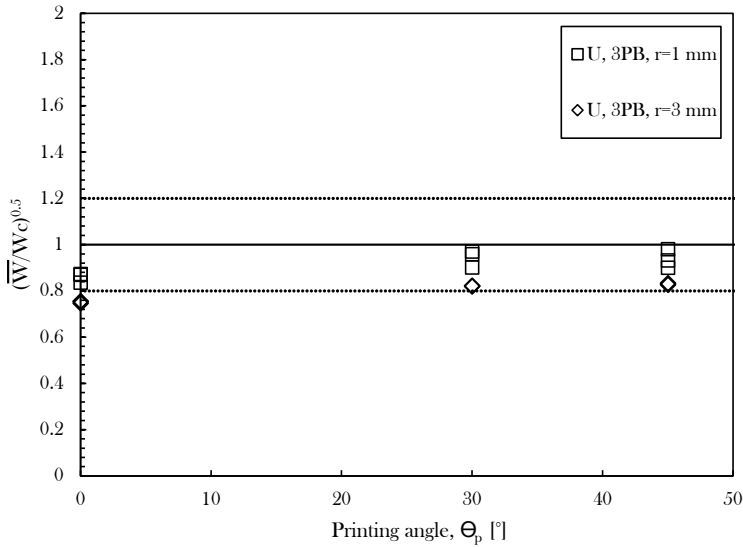
Figure 4.7: Results specimens H and I.

In figure 4.8 the results from specimens G, J, K, and L are presented. These are all V-notched specimens subjected to 3PB testing. These results are those which give the largest consistent deviations. When looking at printing angles 0° and 30° for all specimens, not one of the results are above 0.8. It can also be noted that for 45° printing angle, the mean value of the data points seems to be around 0.8. It is also noticeable that the values for the $r = 0.05mm$ specimens are the most consistent, and also the values which give the best results regardless of printing angle. The $r = 3mm$ specimens are at the opposite side of the scale with values ranging from about 0.65 to a maximum of about 0.75 for all printing angles. Another point to note about this graph, is the fact that the two specimens which seemingly are the most consistent throughout the different printing angles, are those with the smallest and largest notch radius, $r = 0.05mm$ and $r = 3mm$. The other two specimens have a much more significant change of mean value ranging from about 0.7 to 0.9 in $(\overline{W}/W_c)^{0.5}$-value.

In figure 4.9, the analysis result from every specimen is compared to the mean value of the experimental result from the respective sample. This graph shows a general move towards better accuracy as the printing angle moves from 0° to 45°. The values which stand out are those for V-notched 3PB, $r = 0.4mm$. For 0° printing angle, the analytical result is about 40% lower than the mean of the experimental result. This fact is also evident in the other two specimens which resemble this one. Both V-notched and 3PB, but $r = 0.4mm$ and $r = 1mm$. Both these values give an almost as high deviation for 0° printing angle, but give a lot better results for printing angles of 30° and 45°.
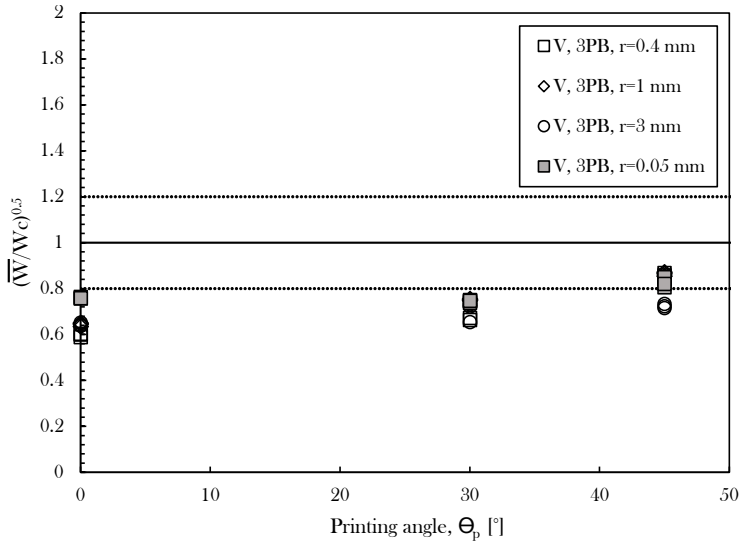
Figure 4.8: Results specimens G, J, K, and L.
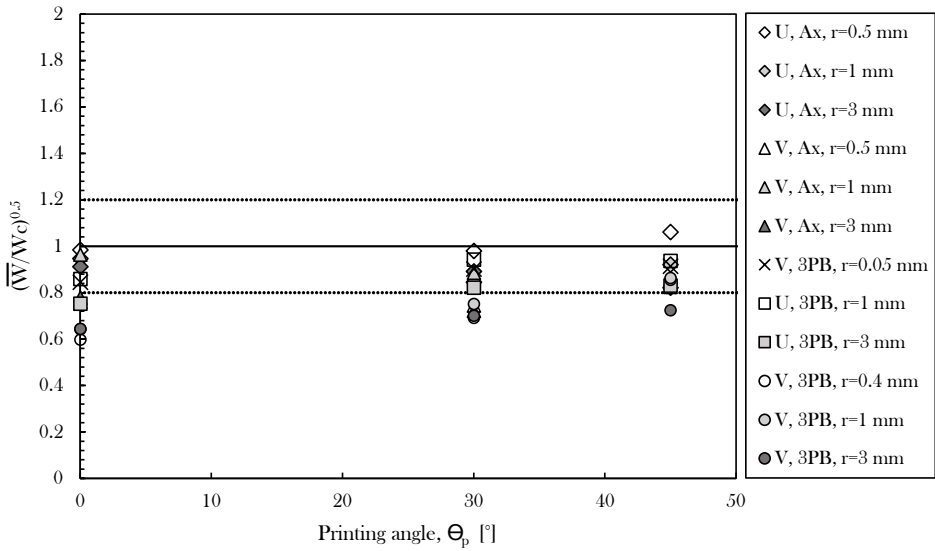
Figure 4.9: Results, all specimens averaged.

4.2.4 Calculating NSIF's and Comparison with Experimental Results

In figure 4.10 (a) through (d), the plotted K-values are shown. It is plotted as a function of the distance from the center of R_2, which is why the values do not start at $r = 0mm$. r is also plotted on a logarithmic scale to give a better presentation of the data, and make it easier to extract data from it. From figures 4.10 (a) and (b) which are for all the tensile specimens, the K-values are almost constant along the bisector line. This fact makes it easier to trust the values as accurate. Figures 4.10 (c) and (d) which show the 3PB specimens, on the other hand were a lot harder to extract K-values from. Especially the specimens containing the largest notch radius were difficult to determine. When looking at the figures, it is important to note the scale of the plotted K-values, which further implies less accurate results for the 3PB specimens.

(a) Specimens A, B and C.

(b) Specimens D, E and F.

(c) Specimens G, H and I.

(d) Specimens J, K and L.
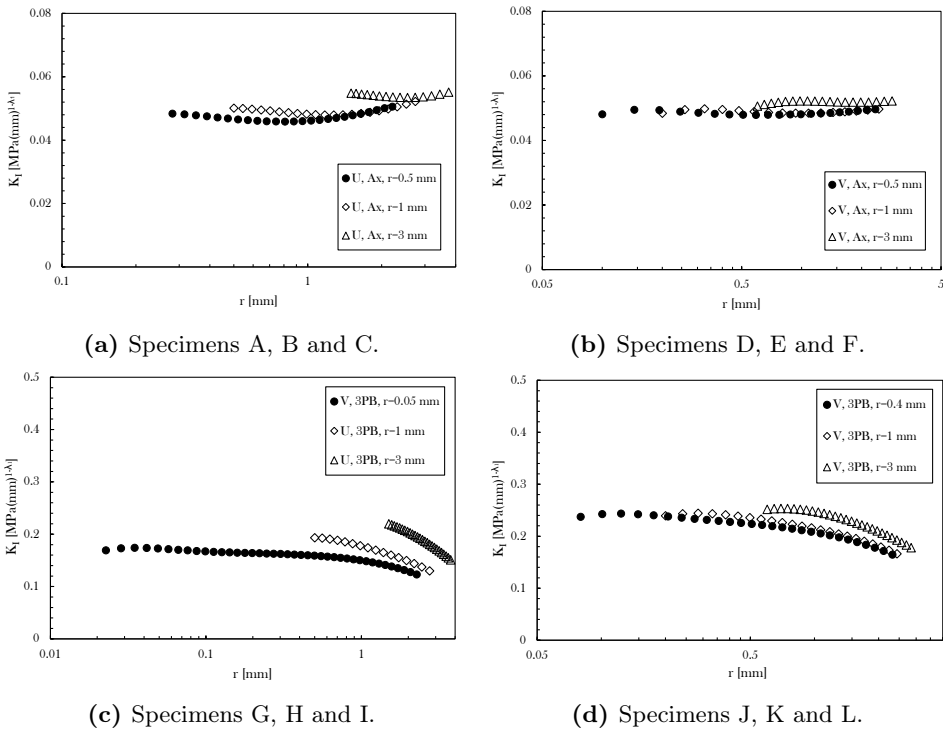
Figure 4.10: The plots from NSIFs for all specimens.

In table 4.6 the K-values for each specimen has been used to estimate a fracture load using equations shown in section 4.1.5. The results from these calculations clearly follow the same trend as the ASED analyses, which is not too surprising, considering the fact that the same FEM models with the same loads and BC's were used, only changing the mesh. The results obtained indirectly from the K-values

however, do have a slightly worse accuracy than the ASED results. The largest deviation between the results obtained from the K-values and those from ASED analyses, are from specimen C, with a 0° printing angle, and specimen H with printing angle 30° and 45°. The difference between these values are at about 10 percent points for both of them.

One important fact to note from the results presented in the table, is that the fracture loads calculated using the second method, which included more factors, generally provided better results. The percent deviation for the second method gives a better percent-wise result by about $2-5$ percent points for every specimen.

Table 4.6: Result from calculating fracture load from NSIF with two different equations and comparison to real fracture load.

Specimen	Print angle [°]	P_{NSIF1} [N]	P_{NSIF2} [N]	P_{exp} [N]	Δ_1[%]	Δ_2[%]
A - U, Ax, r=0.5mm	0	2917	3094	3221	-9	- 4
	30	2509	2662	2833	-11	- 6
	45	2679	2842	2784	-4	2
B - U, Ax, r=1mm	0	2765	2933	3331	-17	- 12
	30	2379	2523	3265	-27	- 23
	45	2539	2694	3187	-20	- 15
C - U, Ax, r=3mm	0	2516	2669	3310	-24	- 19
	30	2164	2296	2930	-26	- 22
	45	2310	2451	3391	-32	- 28
D - V, Ax, r=0.5mm	0	2423	2514	3319	-27	- 24
	30	2194	2277	3078	-29	- 26
	45	2327	2415	2944	-21	- 18
E - V, Ax, r=1mm	0	2468	2561	2790	-12	- 8
	30	2203	2286	2635	-16	- 13
	45	2336	2424	2886	-19	- 16
F - V, Ax, r=3mm	0	2321	2408	3236	-28	- 26
	30	2071	2149	3135	-34	- 31
	45	2197	2280	2898	-24	- 21
G - V, 3PB, r=0.05mm	0	789	845	1040	-24	- 19
	30	679	727	829	-18	- 12
	45	724	776	875	-17	- 11
H - U, 3PB, r=1mm	0	779	826	1067	-27	- 23
	30	670	711	827	-19	- 14
	45	715	759	890	-20	- 15
I - U, 3PB, r=3mm	0	713	757	1136	-37	- 33
	30	614	651	874	-30	- 25
	45	655	695	927	-29	- 25
J - V, 3PB, r=0.4mm	0	542	562	1000	-46	- 44
	30	484	502	754	-36	- 33
	45	513	532	649	-21	- 18
K - V, 3PB, r=1mm	0	551	572	927	-41	- 38
	30	492	511	693	-29	- 26
	45	522	542	642	-19	- 16
L - V, 3PB, r=3mm	0	538	558	899	-40	- 38
	30	480	498	722	-34	- 31
	45	509	528	744	-32	- 29

5 | Discussion

The analyses conducted using the ASED approach consistently gave low results. The scatter of the results were not deemed to be the most significant problem, because only a few results fell outside the $0.8 - 1.2$ scatter band. This can imply that some modifications to the analyses possibly can increase the mean value of the results, thus increasing the accuracy of the results.

One hypothesis to explain the low values of the results is an inaccurate fracture toughness value (K_{IC}). As mentioned by Berto and Lazzarin (2014), the fracture toughness is very sensitive to variations in the notch radii. Notch root radius of too high values are known to give artificially high K_{IC} values as well (Damani et al. (1996)). The AM method, FDM, has limitations when it comes to fine details and printing very sharp notches. Ahmed and Susmel (2018) chose not to create sharper notch root radii to the test specimens than the direct print would give. Part of the reason for doing this, was to study how accurate K_{IC}-values one can obtain from as-printed specimens.

Also, the article authors pointed out the fact that the crack initiation point was not at the exact notch tip for every CT specimen. Especially the specimens printed at angles other than $45°$, which leaves the filaments laying perpendicular and longitudinal to the loading direction. This is a natural result of not creating a sharper crack.

The fact that the K_{IC} values were inaccurate was also pointed out by Ahmed and Susmel (2018). In fact, it was chosen not to use the values obtained from their own analyses, which is explained in section 3.1.2. An alternative method, which calculated L for the TCD calculations using the point method was used. This was done through post-processing the local stress fields of a U-notched specimen.

By post-processing the value for K_{IC} using equation 3.2, the equation for calculating the L-value, a higher K_{IC} was obtained. Through increasing this value, the control radius is increased, due to the nature of equation 2.11. A higher control radius will naturally decrease the density of the strain energy since areas further away from the notch are included. This will in turn lead to a higher predicted failure load. This can indicate that finding an alternate way of calculating K_{IC} can be one way of improving the results from the ASED analyses.

It is also worth noting that by creating a sharper crack for the C(T) specimens, it is highly likely that a lower value K_{IC} will be obtained, which in turn works against improving the immediate results from the ASED analysis. This however, would

have to be tested, and is one of the next natural steps in learning to understand the failure mechanisms of AM PLA.

The Poisson's ratio which was used for all the specimens was obtained from literature on bulk PLA. The different printing angles will likely have an effect on the ratio, because of the anisotropy. It is also likely that the different printing angles will cause different Poisson's ratios for the different directions. For plane problems like the case in this thesis, values for Poisson's ratio for the two unit directions could be beneficial. The Poisson's ratio is the only material property along with the elastic modulus which gives the elastic behaviour of the material. One can therefore assume that it can have an effect on results obtained.

The fracture mechanisms for specimens created using FDM will have an internal structure which is quite different from specimens created from moulding. Figure 2.8 shows the internal structure of typical FDM parts. The images of fracture surfaces from tested specimens in Ahmed and Susmel (2018), show that the path of the fracture is highly dependent on the printing angle. This can indicate local mixed modes caused by the filament directions not being aligned with the loading direction. Through the different material properties obtained from the different angles as well, it is safe to assume that the printing angle has a large effect on the strength of the geometry.

For the specimens tested in uniaxial tension, the overall trend for the experimental results, are highest strength for the 0° printing angle, lower for 30° and lowest for 45°. For the 3 point bending test, highest strength is also observed in the 0° specimens, but 30° and 45° seem rather arbitrary as to which has the highest strength.

Another point to note is that in all the graphs in figures 4.5 through 4.8, it is evident that the specimens printed at 45° generally give better results than the other printing angles. This is visible because the 45° specimens have a mean value which is closer to 1 than the other specimens of the same geometry, but different printing angles. This is also visible in figure 4.9, which is an overview of all the specimens.

The fact that 45° printed specimens give better overall results, can possibly be explained by the elasticity, or rather, the lack of ductility in the material. The ASED approach is predominantly an approach for brittle or quasi-brittle materials, as it is based on the theory that a critical value of decohesive stress within a damaged area will cause failure (Seweryn (1994), Lazzarin and Zambardi (2001)). However, recently, an energy based approach has been successfully applied in problems concerning plasticity (Torabi et al. (2017a), Torabi et al. (2017b)), but will not be included in this thesis. The stress strain curves of the different printing angles from Ahmed and Susmel (2018) can give some indications as to what type response the different angles have. The specimens printed at 0° clearly have a more ductile response to uniaxial tensile loading. The specimens printed at 30° and 45° both have a more brittle behaviour.

Explaining this difference in response, might be done by the fact that the filaments in the 0° specimens can straighten or align somewhat with the loading

direction before failure. The 45° specimens already have every other layer of filaments aligned with the loading direction. Another factor is the fact that PLA is considered a brittle material. Thus, when these specimens fail, it is solely due to a critical state in the material, causing a sudden rupture. Keeping in mind the areas of use for the ASED criterion, it can be argued that this is a contributing factor to the more accurate results obtained from the specimens printed at 45°.

The results from the 3 point bending specimens generally gave a worse correlation with experimental results obtained for the same samples than the uniaxial specimens. The 3PB specimens printed at 0° however, were by far the specimens which gave the worst results. From the tables presenting the results from both the ASED and NSIF analyses (tables 4.5 and 4.6), the higher strength of the experimental tests of these specimens are evident. For the axial specimens, the percentage deviation between printing angle 0° and the other two, varies from 1% to 15%. The 3PB specimens however, deviate consistently with around 20%.

The results from the analyses do not follow this trend. This is quite visible in both the tables and graphs presenting the results of the analyses compared to the experimental results. In figures 4.7 and 4.8 which look at the 3PB specimens, a large portion of the plots are not inside the $0.8 - 1.2$ scatter. This is especially valid for the V-notched specimens (figure 4.8).

There can be several reasons for this. One hypothesis is that the 0° printing angle, which leaves filaments at 45° angles to the loading direction, gives an advantage when subjected to 3PB loading. The 3PB samples G, H, and I, all have a length of $60mm$. Symmetry conditions give that the filaments at an angle of 45° from the point of the applied load will end up at the exact point where the two supports are located. This is illustrated in figure 5.1. For samples J, K and L which all have lengths of $70mm$, they will end up $5mm$ inside both supports. This fact allows stresses to be distributed through the length of filaments, which is beneficial to stresses flowing across the length of the filaments. This can be a contributing factor to the abnormal high strength of these samples.

Accounting for the effects of the direction of the filaments when solely applying material properties obtained from tensile testing is difficult. The results from the analyses conducted, can imply that the the specimens react different under compression than tension as well, which further complicates the case.
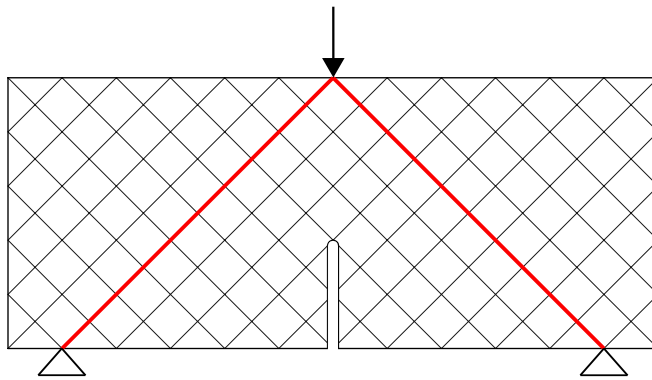
Figure 5.1: Principle drawing of filament direction and loading of 3PB specimens with
0° printing angle.

6 | Conclusion

The objectives states in chapter 1, gave the basis and framework for this thesis. An energy-based approach to analytically predict failure loads of 3D-printed PLA specimens was conducted. The analyses results, which for the most part are within a scatter band of -20% to 20% deviation from the experimental results, indicate that the method is sound. However, the mean value of the results are consistently low, providing non-conservative predictions.

Results showed that the energy-based analyses are relatively mesh size independent. It has also been showed that an approach where the stress intensity factors are plotted, give results which correlate quite well with the results from the energy-based approach.

In short, the use of ASED on additively manufactured PLA specimens is shown to be functional, however, not entirely accurate. The advantages of the energy approach, considering time consumption and computational capacity, possibly outweighs the disadvantages when it comes to accuracy and detail. Therefore, it can be considered a reasonable investment in the future of fracture mechanics to study this field more.

Further Work

There are several points which need improving or researching before the ASED approach can be considered trustworthy for geometries printed using FDM in PLA. First, a better understanding of how the printing angle affects the material properties is needed. This includes determining the Poisson's ratio for different directions through experimental testing, as well as the elastic modulus. Also, using recent developments into the use of energy-based approaches to predicting fracture, where plasticity in the material is included, requires further research.

Second, the fracture toughness of the 3D-printed specimens are not understood well enough. Several experiments using different pre-cracked specimens should be conducted to provide empirical data. Using the different fracture toughness in ASED analyses to see which gives the best correlation with the experiments could be one way of determining the accuracy.

Lastly, studying the reason behind the problem of the analytical results being consistently lower than the experiments could give better insight into the contributing factors. It has been suggested in this thesis that the fracture toughness could be one of the main contributors to this. However, those claims require more research.

Bibliography

Ahmed, A., Susmel, L., 2018. A material length scale-based methodology to assess static strength of notched additively manufactured polylactide (PLA). Fatigue & Fracture of Engineering Materials & Structures (October 2017), 1–28.

Ahn, S., Montero, M., Odell, D., Roundy, S., Wright, P. K., 2002. Anisotropic material properties of fused deposition modeling ABS. Rapid Prototyping Journal 8 (4), 248–257.

Aliha, M., Berto, F., Mousavi, A., Razavi, S., 2017. On the applicability of ased criterion for predicting mixed mode i+ ii fracture toughness results of a rock material. Theoretical and Applied Fracture Mechanics 92, 198–204.

Anderson, T. L., 2005. Fracture Mechanics: Fundamentals and Applications, 3rd Edition. CRC press.

Ayatollahi, M., Aliha, M., 2011. On the use of an anti-symmetric four-point bend specimen for mode ii fracture experiments. Fatigue & Fracture of Engineering Materials & Structures 34 (11), 898–907.

Berto, F., Lazzarin, P., 2009. A review of the volume-based strain energy density approach applied to v-notches and welded structures. Theoretical and Applied Fracture Mechanics 52 (3), 183–194.

Berto, F., Lazzarin, P., 2014. Recent developments in brittle and quasi-brittle failure assessment of engineering materials by means of local approaches. Materials Science and Engineering: R: Reports 75, 1–48.

Damani, R., Gstrein, R., Danzer, R., 1996. Critical notch-root radius effect in senb-s fracture toughness testing. Journal of the European Ceramic Society 16 (7), 695–702.

Dassault Systèmes Simulia, 2014. Abaqus 6.14 CAE User Guide, 1146.

Garlotta, D., 2001. A literature review of poly (lactic acid). Journal of Polymers and the Environment 9 (2), 63–84.

Hosford, W. F., 2005. Mechanical Behavior of Materials. Cambridge university press.

Kariduraganavar, M. Y., Kittur, A. A., Kamble, R. R., 2014. Polymer synthesis and processing. In: Natural and Synthetic Biomedical Polymers. Elsevier, pp. 1–31.

Kirsch, G., 1896. Die theorie der elastizitaet und die beduerfunisse der festigkeit-slehre (theory of elasticity and application in strength of materials). Zeitschrl/t Verein Deutscher Ingenieure 42 (29), 797–807.

Lazzarin, P., Berto, F., Zappalorto, M., 2010. Rapid calculations of notch stress intensity factors based on averaged strain energy density from coarse meshes: Theoretical bases and applications. International Journal of Fatigue 32 (10), 1559–1567.

Lazzarin, P., Filippi, S., 2006. A generalized stress intensity factor to be applied to rounded V-shaped notches. International Journal of Solids and Structures 43 (9), 2461–2478.

Lazzarin, P., Zambardi, R., 2001. A finite-volume-energy based approach to predict the static and fatigue behavior of components with sharp V-shaped notches. International Journal of Fracture 112 (3), 275–298.

Otani, L. B., Segundinho, P. G. d. A., Morales, E. A. M., Pereira, A. H. A., 2015. Elastic moduli characterization of wood and wood products using the Impulse Excitation Technique. ATCP physical engineering 1 (February), 33.

Radaj, D., Lazzarin, P., Berto, F., 2009. Fatigue-relevant stress field parameters of welded lap joints: pointed slit tip compared with keyhole notch. Fatigue & Fracture of Engineering Materials & Structures 32 (9), 713–735.

Razavi, S. M., Aliha, M. R., Berto, F., 2017. Application of an average strain energy density criterion to obtain the mixed mode fracture load of granite rock tested with the cracked asymmetric four-point bend specimens. Theoretical and Applied Fracture Mechanics.

Seweryn, A., 1994. Brittle fracture criterion for structures with sharp notches. Engineering Fracture Mechanics 47 (5), 673–681.

Susmel, L., Taylor, D., 2008. On the use of the theory of critical distances to predict static failures in ductile metallic materials containing different geometrical features. Engineering Fracture Mechanics 75 (15), 4410–4421.

Tada, H., Paris, P. C., Irwin, G. R., 1973. The stress analysis of cracks. Handbook, Del Research Corporation.

Torabi, A., Berto, F., Razavi, S., 2017a. Ductile failure prediction of thin notched aluminum plates subjected to combined tension-shear loading. Theoretical and Applied Fracture Mechanics.

Torabi, A., Berto, F., Razavi, S., 2017b. Tensile failure prediction of u-notched plates under moderate-scale and large-scale yielding regimes. Theoretical and Applied Fracture Mechanics.

Torres, J., Cotelo, J., Karl, J., Gordon, A. P., 2015. Mechanical property optimization of FDM PLA in shear with multiple objectives. Jom 67 (5), 1183–1193.

Wang, X., Jiang, M., Zhou, Z., Gou, J., Hui, D., 2017. 3D printing of polymer matrix composites: A review and prospective. Composites Part B: Engineering 110, 442–458.

Williams, M., 1952. Stress singularities resulting from various boundary conditions in angular corners of plates in extension. Journal of applied mechanics 19 (4), 526–528.

Appendix

Table 6.1: ELSE, EVOL, and resulting ASED values obtained from analyses.

Specimen	Print angle [°]	ELSE [mJ]	EVOL [mm^3]	ASED [mJ/mm^3]
A - U, Ax, r=0.5mm	0	5,56E-06	199,39	2,79E-08
	30	4,29E-06	131,96	3,25E-08
	45	4,39E-06	141,63	3,10E-08
B - U, Ax, r=1mm	0	5,86E-06	207,66	2,82E-08
	30	4,55E-06	138,08	3,29E-08
	45	4,65E-06	148,08	3,14E-08
C - U, Ax, r=3mm	0	6,94E-06	225,45	3,08E-08
	30	5,48E-06	149,38	3,67E-08
	45	5,58E-06	160,30	3,48E-08
D - V, Ax, r=0.5mm	0	4,97E-06	120,45	4,12E-08
	30	3,63E-06	79,22	4,58E-08
	45	3,75E-06	85,13	4,41E-08
E - V, Ax, r=1mm	0	5,88E-06	151,80	3,88E-08
	30	3,74E-06	81,47	4,59E-08
	45	3,86E-06	87,45	4,41E-08
F - V, Ax, r=3mm	0	5,75E-06	130,10	4,42E-08
	30	4,26E-06	87,21	4,88E-08
	45	4,39E-06	93,38	4,70E-08
G - V, 3PB, r=0.05mm	0	3,23E-05	88,92	3,63E-07
	30	2,61E-05	58,30	4,48E-07
	45	2,65E-05	62,68	4,23E-07
H - U, 3PB, r=1mm	0	3,56E-05	106,47	3,34E-07
	30	2,92E-05	70,79	4,12E-07
	45	2,95E-05	75,92	3,89E-07
I - U, 3PB, r=3mm	0	4,32E-05	112,75	3,84E-07
	30	3,63E-05	74,64	4,86E-07
	45	3,66E-05	80,08	4,57E-07
J - V, 3PB, r=0.4mm	0	4,70E-05	59,95	7,85E-07
	30	3,63E-05	39,41	9,20E-07
	45	3,71E-05	42,35	8,77E-07
K - V, 3PB, r=1mm	0	4,86E-05	61,62	7,88E-07
	30	3,76E-05	40,74	9,23E-07
	45	3,85E-05	43,73	8,80E-07
L - V, 3PB, r=3mm	0	5,45E-05	65,05	8,38E-07
	30	4,26E-05	43,60	9,78E-07
	45	4,35E-05	46,69	9,33E-07